

1 Integration of sleep homeostasis and navigation in 2 *Drosophila*

3 Andres Flores Valle¹, Pedro J. Gonçalves^{2,3,*}, and Johannes D. Seelig^{1,*}

4 ¹Center of Advanced European Studies and Research (caesar), Bonn, Germany

5 ²Max Planck Research Group Neural Systems Analysis, Center of Advanced European Studies and Research
6 (caesar), Bonn, Germany

7 ³Computational Neuroengineering, Department of Electrical and Computer Engineering, Technical University of
8 Munich, Germany

9 *pedro.goncalves@caesar.de

10 *johannes.seelig@caesar.de

11 ABSTRACT

During sleep, the brain undergoes dynamic and structural changes. In *Drosophila*, such changes have been observed in the central complex, a brain area important for sleep control and navigation. The connectivity of the central complex raises the question about how navigation, and specifically the head direction system, can operate in the face of sleep related plasticity.

12 To address this question, we develop a model that integrates sleep homeostasis and head direction. We show that by introducing plasticity, the head direction system can function in a stable way by balancing plasticity in connected circuits that encode sleep pressure. With increasing sleep pressure, the head direction system nevertheless becomes unstable and a sleep phase with a different plasticity mechanism is introduced to reset network connectivity.

The proposed integration of sleep homeostasis and head direction circuits captures features of their neural dynamics observed in flies and mice.

13 1 Introduction

14 Sleep affects many different brain functions such as cognition¹ or working memory² and sleep dysfunction is related to a range of diseases³. Sleep is observed across species and different hypotheses have been put forward to explain the function of sleep⁴, for example reverse learning of spurious network states (that were created as a byproduct of intended memories)⁵⁻⁷ or weakening of synapses (synaptic homeostasis hypothesis)⁸.

15 The function of sleep is linked to the dynamic and structural changes that it induces in the brain⁹, which in turn are monitored by sleep control or sleep homeostasis circuits^{10,11}. The circuits that control sleep are distributed over many different brain areas and cell types¹⁰. Thanks to the genetic tools^{12,13} that allow dissecting neural circuits into small populations of genetically identified cell types, as well as more recently the fly connectome¹⁴, *Drosophila* has emerged as a valuable model for sleep control^{11,15-17}.

16 A generic sleep control circuit has been linked to specific neural populations in the brain of *Drosophila* in¹⁸. This circuit has three components and corresponding neural populations in the central complex (Figure 1A). A first component encodes sleep pressure. The corresponding neural population has been identified in the so called R5 ring neurons which arborize in concentric rings in the ellipsoid body¹⁹, a substructure of the central complex. These R5 neurons increase both their activity and synaptic strength over waking time and are reset with sleep. A second component of the sleep control circuit executes the switch between sleep and wakefulness (depending on the amount of sleep pressure). The corresponding neural population has been associated with the the dorsal fan-shaped body (dFB) neurons, which promote sleep when active²⁰. A third component triggers locomotion, processes visual input, and increases sleep pressure¹⁸ and the corresponding neurons are so called helicon cells¹⁸, also identified as ExR1 neurons²¹. The proposed recurrent circuit between these three neural populations¹⁸ is illustrated in Figure 1A.

17 The same central complex structures involved in sleep have also been shown to be important for navigation.

34 In particular, ring neurons with similar morphology to the sleep-related R5 ring neurons, provide sensory input to
35 the head direction system, such as visual features^{22,23} or wind direction²⁴. Such input is integrated in so called
36 wedge neurons, which arborize in different wedges of the ellipsoid body, where they intersect with ring neurons.
37 These wedge neurons encode the head direction of the fly through a bump of activity that moves around the ellipsoid
38 body²⁵.

39 In the context of navigation, the structure and function of circuits in the central complex are reminiscent of ring
40 attractor networks²⁵. Such networks, which are well suited to encode a circular variable, have been suggested to
41 underlie the encoding of head direction, originally in mammals²⁶ and more recently in flies²⁵.

42 It is currently unknown why the circuits for sleep homeostasis and head direction converge in the central complex.
43 The morphological similarity of the ring neurons involved in sleep and head direction and the spatial proximity of
44 the circuits as well as the fly connectome¹⁴, suggest that they interact. Given the observed activity and structural
45 changes in R5 ring neurons after prolonged waking time and after sleep^{19,27,28}, this suggests that the head direction
46 system in the ellipsoid body needs to operate in the face of substantial synaptic and functional changes in connected
47 circuits.

48 Motivated by this interaction between navigation and sleep homeostasis circuits as well as their plasticity^{19,27,28},
49 we here use theoretical modeling to investigate how these two circuits can be understood as a combined system.
50 For this purpose, we first model the circuit proposed in¹⁸ and confirm that it generates sleep homeostasis. We then
51 extend the model by combining it with a head direction network as suggested by the connectome. In this combined
52 model, the sleep pressure encoding R5 neurons balance Hebbian plasticity introduced in the recurrent connections of
53 the head direction system. In this way, ring neurons maintain a functioning head direction system and record sleep
54 pressure. The system is finally reset through a sleep phase.

55 We discuss how this model can integrate several experimental observations on the navigation and sleep home-
56 ostasis systems reported in the literature. We further discuss several predictions of the model that can be tested in
57 experiments. This analysis contributes to an understanding of the generation and dynamics of sleep drive and links
58 the control of sleep to sleep function.

59 2 Results

60 2.1 Sleep homeostasis model

The sleep homeostasis model proposed in¹⁸ is illustrated in Figure 1A. All connections between populations are
direct¹⁸, except the connection between R5 and dFB neurons, which is considered indirect since these neural popula-
tions are not anatomically, but functionally connected¹⁹. This circuit is described by the following phenomenological
model:

$$\begin{cases} \tau_I \dot{r}_I(t) = -r_I(t) + r_{ExR1}(t) \\ \tau \dot{r}_{ExR1}(t) = -r_{ExR1}(t) + 1 - r_{dFB}(t) \\ \tau \dot{r}_{dFB}(t) = -r_{dFB}(t) + [G(r_I) - d(t)]_+ \end{cases} \quad (1)$$

61 The variables $r_I(t)$, $r_{ExR1}(t)$ and $r_{dFB}(t)$ represent population firing rates of R5 neurons, ExR1 neurons and dFB
62 neurons, respectively. The time constant τ_I accounts for the slow dynamics of increasing activity observed during
63 waking time in R5 neurons¹⁹ on the order of hours. The effective population time constant τ accounts for neural
64 dynamics in the millisecond range. $[\cdot]_+$ is a threshold-linear function to ensure positive-valued firing rates. For
65 simplicity, the model is defined such that population firing rates are between 0 and 1. The variable $d(t)$, which
66 can take values 0 or 1, represents an input to dFB neurons such as a wake-promoting dopaminergic signal²⁹. The
67 function $G(r_I)$, which depends on the history of activity of R5 neurons and produces the observed switching behavior
68 in dFB neurons¹⁸, is described with a simple hysteresis (equation (9)).

69 Figure 1B shows a simulation of this model with the firing rates of the different populations changing over
70 time. The sleep and wake phases are defined in terms of the activity of dFB neurons, which promote sleep while
71 active²⁰. During the wake phase, activity in R5 neurons increases, encoding sleep pressure due to sustained constant
72 input from ExR1 neurons. After ring neurons reach an upper threshold, $r_I^{(max)}$, dFB neurons 'switch on' and inhibit

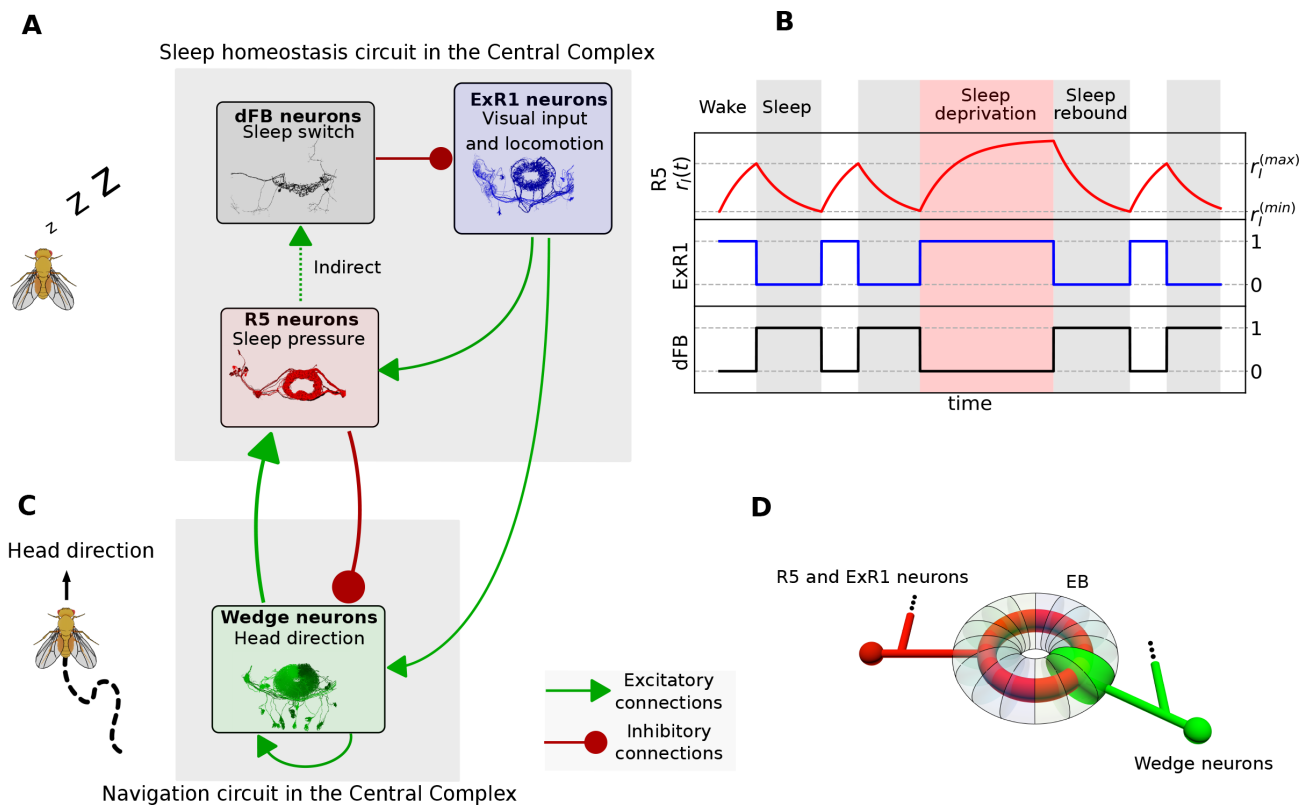


Figure 1. Sleep homeostasis and navigation circuits in the central complex. **A** Recurrent sleep homeostasis circuit proposed in¹⁸. The three populations are connected via excitatory (green arrows) or inhibitory (red arrows) connections. **B** Simulation of the sleep homeostasis model illustrating the dynamics of each population over time. **C** Interaction between the fly head direction circuit and populations involved in sleep homeostasis. **D** Schematic of connectivity between wedge neurons and R5 and ExR1 neurons in the ellipsoid body. Images are downloaded from the connectome database¹⁴.

73 activity in ExR1 neurons, which leads to a decrease in activity of R5 neurons. Once R5 activity reaches a lower
 74 threshold, $r_i^{(min)}$, dFB neurons switch off, repeating the cycle. Sleep deprivation (by setting $d(t) = 1$ in the top red
 75 region) inhibits activity of dFB neurons and activity of ring neurons increases beyond $r_i^{(max)}$. As expected for a sleep
 76 homeostasis circuit, after sleep deprivation, more time is required to reset the activity of R5 neurons back to $r_i^{(min)}$
 77 (sleep rebound, see Methods 4.3 for details of simulation).

78 2.2 Connectivity between head direction and sleep circuits

79 While the circuit described above can produce sleep homeostasis, the connectome¹⁴ shows that it acts not in isolation
 80 but interacts with the head direction system. Figure 1A and C show how R5 and ExR1 neurons are connected to
 81 wedge neurons that encode head direction. The anatomical organization of wedge, R5 and ExR1 neurons is shown
 82 schematically in Figure 1D, where each wedge neuron arborizes in a different wedge along the ellipsoid body,
 83 and R5 and ExR1 neurons arborize in concentric rings. The wedge neurons that encode head direction have been
 84 identified as EPG neurons²⁵, but a similar population of wedge neurons, called EL^{14,30} or AMPG-E³¹, could also
 85 potentially encode head direction. These neurons have been proposed to contribute to the persistent activity in the
 86 network by excitatory feedback to EPG neurons³¹. These neurons can mediate a connection between R5 and EPG
 87 neurons that is stronger than the direct connection between R5 and EPGs. In the following, wedge neurons refer to
 88 both EPG or EL populations without distinction. We assume that both encode head direction and are directly or
 89 indirectly connected to R5 neurons. In Figure S1, we show recurrent connections between wedge neurons (Figure

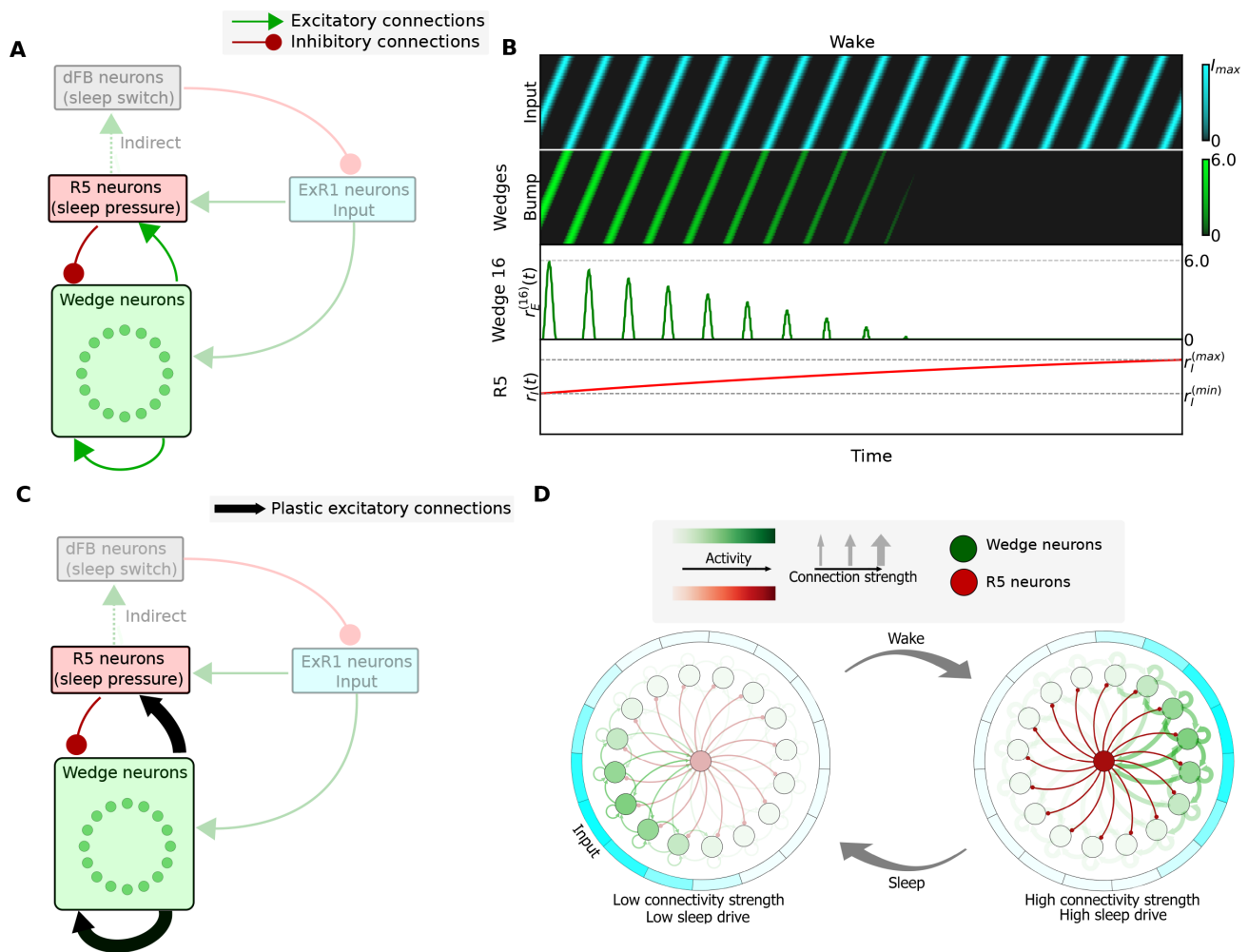


Figure 2. Integration of the sleep homeostasis circuit with a ring attractor network. **A** Schematic of a model where wedge neurons are connected to the sleep homeostasis circuit according to the fly connectome (see Figure S1). In this model, fixed connections are assumed. **B** Simulation of the model in A (dFB neurons not shown). Top row: rotating input to the ring attractor with a frequency 0.5 Hz. Second row: bump of activity in wedge neurons encoding head direction. Third row: activity of the wedge neuron 16 (representative for any other wedge neuron). fourth row: increasing activity of R5 neurons. **C** Model with plastic connections indicated by black arrows. **D** Dynamics of the model with plasticity: after a wake phase, high connectivity strength in the ring attractor leads to high sleep drive in R5 neurons, which leads to a switch to the sleep phase. After sleep, connectivity strength in the ring attractor is reset, producing low sleep drive.

90 S1A), between wedge and R5 neurons (Figure S1B)), and between wedge and ExR1 neurons (Figure S1C) according
 91 to the connectome¹⁴.

92 2.3 Integration of sleep homeostasis and ring attractor circuits without plasticity

93 The interaction of the sleep homeostasis and ring attractor circuits extracted from the fly connectome is shown
 94 schematically in Figure 2 A. Given that R5 neurons and wedge neurons are bidirectionally connected (see Figure
 95 S1B), we first asked how increasing activity of R5 neurons during the wake phase (see Figure 1B, first row)
 96 affects the head direction network. We therefore combined a ring attractor network with the above sleep homeostasis
 97 model (section 2.1) according to the connectivity in Fig. 2 A. As in previous work^{32,33}, we identify wedge neurons
 98 as the excitatory component of a ring attractor network with recurrent excitation, encoding head direction with

99 sustained bump-like activity. On the other hand, we assume that R5 neurons provide increasing inhibition to wedge
 100 neurons³⁴, in agreement with the majority of ring neurons being inhibitory^{35,36}. (For simplicity, we assume that
 101 ExR1 neurons, which are bidirectionally connected to wedge neurons, provide input to the ring attractor similar to
 102 other ring neurons, and that wedge neurons and not ExR1 neurons, as suggested in¹⁸, charge the sleep homeostat.)

103 Figure 2B shows the activity of wedge neurons and R5 neurons with a rotating input, representing visual or
 104 idiothetic cues, (in blue, first row) which as expected moves the bump around the ring attractor (in green, second
 105 row). Increased activity in R5 neurons, as experimentally observed with increased sleep drive, decreases the bump
 106 amplitude in the ring attractor until it finally vanishes. Therefore, simply connecting R5 and wedge neurons as
 107 indicated by the connectome, leads to a decreasing bump of activity over time.

108 2.4 Integration of sleep homeostasis and ring attractor circuits with plasticity

109 In Figure 2C, we propose an alternative model that can sustain a stable bump amplitude. In order to overcome a
 110 decreasing bump amplitude (which has not been experimentally observed), we hypothesize that the increase of
 111 inhibition from R5 neurons, in addition to encoding sleep drive, has the role of compensating for an increase in
 112 excitation in the head direction circuit. In particular, we hypothesize that excitatory synaptic strength between wedge
 113 neurons increases during the wake phase. This could be due to Hebbian plasticity between wedge neurons, since
 114 encoding the head direction in a bump of activity requires several wedge neurons to be active at the same time,
 115 thus strengthening the recurrent connections. This model is additionally motivated by the experimentally observed
 116 increase of activity as well as plasticity in R5 neurons¹⁹. In agreement with these data, we additionally add Hebbian
 117 plasticity from wedge neurons to R5 neurons.

118 In this model, R5 neurons act as a closed-loop feedback controller that prevents activity in wedge neurons from
 119 increasing due to hebbian plasticity, by adaptively increasing inhibition. In the context of the sleep homeostasis
 120 circuit, dFB neurons then detect synaptic growth in R5 neurons. When R5 neural activity reaches an upper threshold,
 121 dFB neurons switch on sleep. We assume that during sleep, the plastic connections are reset with LTD, decreasing
 122 activity in R5 neurons (as observed in¹⁹) and lowering sleep drive (Figure 2D, left).

The network shown schematically in Figure 2C is implemented with $N = 32$ wedge neurons (based on anatomy³⁷).
 For simplicity, we model the population of R5 neurons with a single variable $r_I(t)$ as in the sleep homeostasis model
 (section 2.1). The activities of wedge and R5 neurons are described by the following system of differential equations:

$$\begin{cases} \tau \dot{r}_E^{(i)}(t) = -r_E^{(i)}(t) + \left[\sum_j^N w_{EE}^{(ij)}(t) r_E^{(j)}(t) - w_{EI} r_I(t) + \theta + I^{(i)}(m, t) \right]_+ & \text{for } i = 1, \dots, N \\ \tau \dot{r}_I(t) = -r_I(t) + \left[\sum_j^N w_{IE}^{(j)}(t) r_E^{(j)}(t) \right]_+ \end{cases} \quad (2)$$

123 Here, $r_E(t)$ and $r_I(t)$ are the firing rates at time t of wedge and R5 neurons, respectively, w_{AB} is the synaptic
 124 weight from population B to population A , θ is a constant background input onto wedge neurons, and τ is the
 125 effective population time constant. The matrix $w_{EE}^{(ij)}$ is initialized with a Gaussian function that depends on the
 126 distance between wedge neurons along the ring. The Gaussian has two parameters, the maximum amplitude, $w_{EE}^{(max)}$,
 127 and the standard deviation σ (equation (38) in Methods). Figure 3A illustrates the connectivity from all the wedge
 128 neurons to wedge neuron 16. Additionally, $I^{(i)}(m, t)$ is an input from any modality to each wedge neuron i (for
 129 example (time-varying) visual or idiothetic input). This input encompasses input from ExR1 neurons, that process
 130 visual stimuli¹⁸, as well as from others populations. We assume that this input can be inhibited by dFB neurons,
 131 $r_S(t)$, as in the sleep homeostasis model (section 2.1), and is defined as a Gaussian function where the peak is located
 132 at a given wedge neuron m (equation (39) in Methods).

133 The inhibition of input to wedge neurons during sleep is motivated by the fact that self-motion inputs are not
 134 present, since the fly does not move during sleep. On the other hand, ExR1 neurons, which contribute to visual
 135 processing and locomotion, are inhibited by dFB neurons¹⁸. We hypothesize that other neural populations providing
 136 visual input to the ring attractor²³ might require coincident activity from ExR1 neurons to reliably transmit visual
 137 information. This information might not be transmitted during sleep because of lack of activity from ExR1 neurons.

138 This is consistent with the idea of an increased arousal threshold during sleep, where stronger stimuli are required to
 139 produce a behavioral response³⁸.

The plasticity during the wake phase in recurrent connections between wedge neurons, $w_{EE}^{(ij)}$, and from wedge to R5 neurons, $w_{IE}^{(j)}$ is modeled as follows:

$$\begin{cases} \tau_{EE} \dot{w}_{EE}^{(ij)}(t) = r_E^{(i)}(t) r_E^{(j)}(t) & \text{for } i, j = 1, \dots, N \\ \tau_{IE} \dot{w}_{IE}^{(j)}(t) = r_I(t) r_E^{(j)}(t) (r_E^{(j)}(t) - r_0) & \text{for } j = 1, \dots, N, \end{cases} \quad (3)$$

140 where τ_{EE} and τ_{IE} are time constants, and r_0 is a positive presynaptic threshold. We assume that the dynamics
 141 of the plasticity rules are much slower than the dynamics of neural populations, so that $\tau_{EE}, \tau_{IE} \gg \tau$, producing
 142 long-term plasticity. The synaptic weight between a presynaptic wedge neuron j and a postsynaptic wedge neuron
 143 i is represented by the time dependent matrix element $w_{EE}^{(ij)}(t)$. While the first plasticity rule is a linear Hebbian
 144 rule, the second is a triplet rule with presynaptic threshold; its behavior is similar to the linear Hebbian rule with
 145 presynaptic threshold, but it has a quadratic dependency on the presynaptic activity while ensuring no change in w_{IE}
 146 if neural activity is zero (see derivation in Methods 4.5.1 and in³⁹).

147 The plasticity rules are motivated by the assumption that the observed increase in activity and synaptic strength
 148 in R5 neurons¹⁹ balance the long-term potentiation in recurrent connections of wedge neurons, $w_{EE}^{(ij)}$. The plasticity
 149 rules therefore produce the following effects: (i) The recurrent synaptic connections between wedge neurons,
 150 $w_{EE}^{(ij)}$, as well as the connections between wedge and ring neurons, w_{IE} , get stronger during the wake phase. (ii)
 151 The firing rate of ring neurons r_I increases during the wake phase. (iii) The amplitude of the bump in wedge
 152 neurons (which represents head direction) evolves always towards a constant setpoint, $r_E \rightarrow r_0$. Note that activity
 153 is not constrained to the setpoint, but evolves towards it over time, since the setpoint is a stable fixed point for
 154 wedge neurons. Therefore, the bump amplitude will deviate from the setpoint due to any (for example visual or
 155 self-motion related) input (see Figure S4), consistent with experimentally observed behavior-related changes in
 156 bump amplitude⁴⁰. These plasticity rules avoid the problem of a vanishing bump amplitude, as observed in the
 157 model with fixed connections (see Figure 2A and B).

158 How plasticity can drive the observed increase in R5 neuron activity with sleep pressure^{19,27} is currently
 159 unknown. Since it is the activity of R5 neurons, and not the plasticity, which is hypothesised to trigger sleep^{18,19,27},
 160 our models assume plasticity that directly modifies the activity of R5 neurons linearly (Figures 3C, 4A and 5A) (a
 161 possibility that is consistent with the data in¹⁹).

162 A simplified model consisting of only one excitatory population representing wedge neurons and one inhibitory
 163 population representing R5 neurons is presented in Methods 4.5. Both populations are connected according to Figure
 164 2C, including the plastic connections. This model shows overall similar characteristics to the full ring attractor
 165 network (see also next section).

166 2.5 Analysis of model stability during the wake phase

167 As shown below, the stability of a bump of activity in wedge neuron i is determined by its total excitatory input,
 168 $w_{EE}^{(i,sum)}(t)$ (Figure 3A). Here and in the following, we focus on wedge neuron 16, but the same analysis applies for
 169 all wedge neurons:

$$w_{EE}^{(16,sum)}(t) = \sum_j^N w_{EE}^{(16,j)}(t). \quad (4)$$

170 Figure 3B shows the different dynamic regimes of the bump as a function of the parameters $w_{EE}^{(max)}$ and σ that
 171 determine the values of $w_{EE}^{(ij)}$ (see Methods (4.7) and Figure S6). The colored lines in Figure 3B are isolines of
 172 constant $w_{EE}^{(16,sum)}$, and correspond to the boundaries of distinct dynamics of the bump of activity in wedge neurons.

173 The boundaries are similar to the ones found in the simpler two-population model (Methods 4.5). The bump is
 174 stable around wedge neuron 16 if $1 < w_{EE}^{(16,sum)} < 2$. As the recurrent weights $w_{EE}^{(ij)}$ increase due to LTP during the

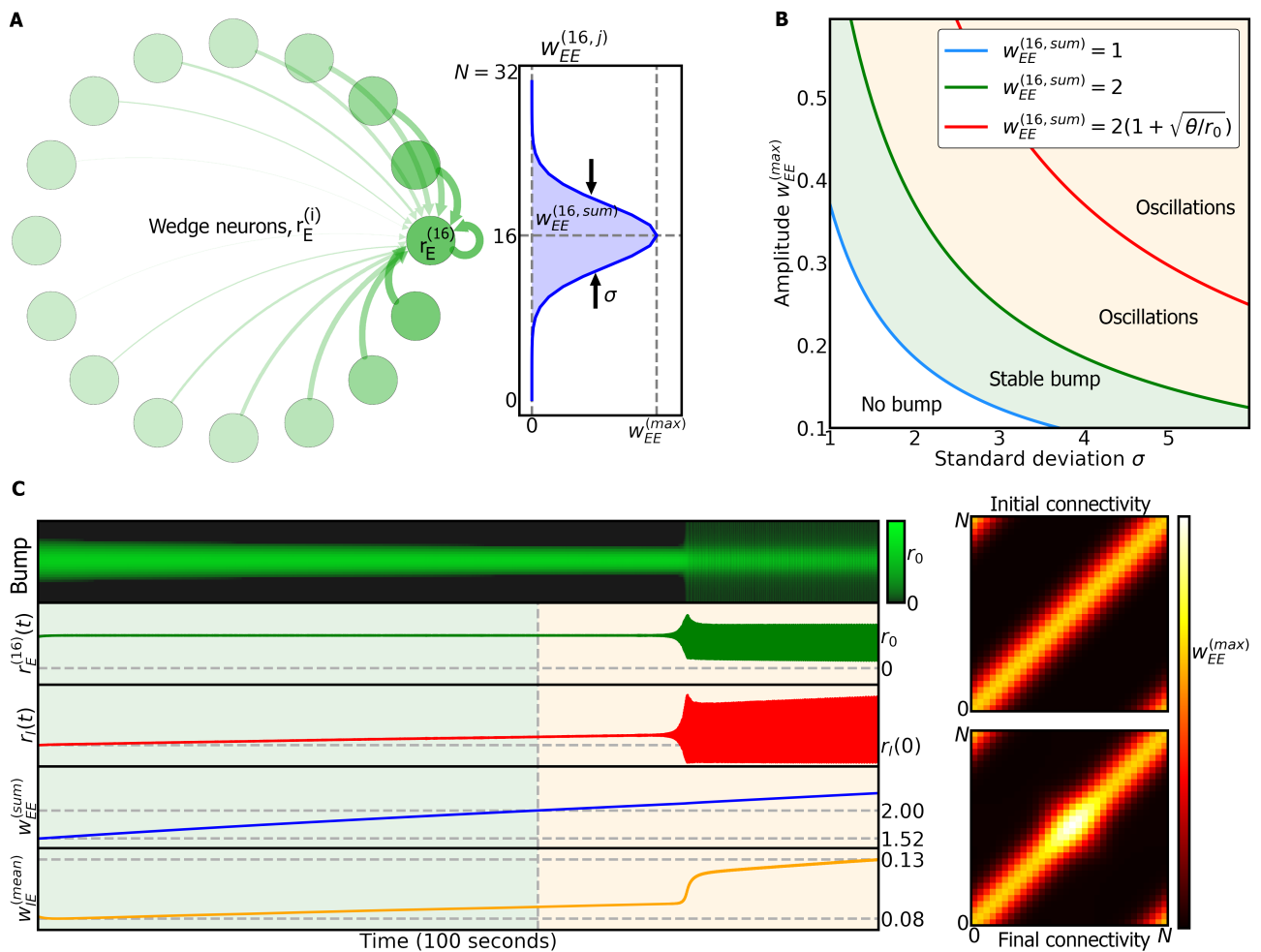


Figure 3. Dynamics of ring attractor network during wake phase. **A** Left side: representation of excitatory connections $r_E^{(i)}$ from all wedge neurons to wedge neuron $r_E^{(16)}$. Right side: Gaussian connectivity from all wedge neurons to wedge neuron 16, with maximum amplitude $w_{EE}^{(max)}$ and standard deviation σ . **B** Model dynamics obtained in the fast-timescale limit (see Methods(4.7)) depend on the parameters of the excitatory connectivity, $w_{EE}^{(max)}$ and σ . **C** Left side: dynamics during wake phase of the ring attractor model where the bump is located around wedge neuron 16. When the total excitatory weight, $w_{EE}^{(16,sum)}$, crosses a threshold, the bump starts to oscillate. Right side, top: initial excitatory connections between wedge neurons. Right side, bottom: final excitatory connections between wedge neurons; changes are a result of synaptic plasticity.

175 wake phase, so do σ and $w_{EE}^{(max)}$. The bump starts to oscillate if recurrent connections are too strong, i.e. $w_{EE}^{(16,sum)} > 2$.
 176 When $w_{EE}^{(16,sum)} > 2(1 + \sqrt{\theta/r_0})$, the bump keeps oscillating with very low activity in wedge neurons (see Methods
 177 4.7).

178 Figure 3C illustrates the dynamics of the system with a bump centered in wedge neuron 16 (first row): as
 179 $w_{EE}^{(16,sum)}$ increases (fourth row) due to Hebbian plasticity, the weights $w_{EE}^{(i)}$ (represented by the mean) also increase
 180 (fifth row), leading to increased activity of R5 neurons (third row), which in turn maintains the amplitude of the
 181 bump in wedge neuron 16 constant (second row).

182 When $w_{EE}^{(16,sum)} > 2$, the bump starts to oscillate, as do R5 neurons (orange region in the last four rows). In
 183 addition, the plasticity rule in the recurrent connections $w_{EE}^{(ij)}$ leads to an increase of the synaptic weights around the

184 bump position (Figure 3C, right side, top vs. bottom).

185 2.6 Resetting the connectivity of the ring attractor during sleep

To limit synaptic growth as well as to avoid the instability of the bump and oscillations in R5 neurons, we introduce a sleep phase, as proposed by models of sleep homeostasis¹⁸. In this model, dFB neurons detect increased activity of R5 neurons and implement the switch between sleep and wake phases. In the model, we use a filtered version of R5 activity, which is motivated by the fact that R5 and dFB are not anatomically but functionally connected¹⁹. Additionally, this filtering prevents uncontrollable switching between phases in the oscillatory regime. The filtered activity of R5 neurons and the activity dFB neurons are modeled as follows:

$$\begin{cases} \tau_f \dot{r}_I^{(f)}(t) = -r_I^{(f)}(t) + r_I(t) \\ \tau \dot{r}_{dFB}(t) = -r_{dFB}(t) + [G(r_I^{(f)}(t)) - d(t)]_+ \end{cases} \quad (5)$$

186 where τ_f is the time constant of the low-pass filter (order of seconds); $r_I^{(f)}$, which we refer to as the switching signal,
187 is a low-pass filter of activity in R5 neurons; and $r_{dFB}(t)$ is the activity of dFB neurons with its switching behavior
188 modeled by equation (9). Finally $d(t)$ is a variable which can produce sleep deprivation.

During the sleep phase, we assume that dFB neurons inhibit input to the ring attractor, similar to the sleep homeostasis model (see equation 39). In addition, our model resets the connectivity strength in $w_{EE}^{(ij)}$ by a change in the plasticity rules during sleep. A simple way to restore the network connectivity $w_{EE}^{(ij)}(t)$ is to relax it to its initial values over the sleep phase:

$$\tau_{EE} \dot{w}_{EE}^{(ij)}(t) = -w_{EE}^{(ij)}(t) + w_{EE}^{(ij)}(0) \quad \text{for } i, j = 1, \dots, N. \quad (6)$$

189
190 Note that we do not change the plasticity rule of $w_{IE}^{(i)}(t)$, since this rule ensures $w_{IE}^{(i)}(t)$ to always follow the trend
191 (potentiation or depression) of $w_{EE}^{(i)}(t)$ in order to maintain the bump amplitude at a setpoint. Figure 4A shows a
192 simulation of the combined ring attractor and sleep homeostasis models ((section 2.1)) with plasticity. During wake
193 phases (top, white region), dFB neurons are inactive ($r_{dFB}(t) = 0$, not shown), and during sleep phases (grey region)
194 dFB neurons are active ($r_{dFB}(t) = 1$). In the wake phase, a rotating input with a constant frequency of 0.5Hz is
195 provided; the input reverses direction between consecutive wake phases (top row). During the wake phase, the bump
196 in the ring attractor closely follows the input (second row), while the activity of R5 neurons increases (light red line
197 in the fourth row). The second to last row shows the diagonal elements of $w_{EE}^{(ij)}$ while the last row shows $w_{IE}^{(i)}$. When
198 the switching signal reaches the upper threshold, $r_I^{(max)}$, dFB neurons switch the model to the sleep phase, where the
199 plasticity rule in $w_{EE}^{(i)}(t)$ changes and input to wedge neurons is inhibited (Figure 4B). During sleep, the bump in
200 wedge neurons stays in place, maintaining the last head direction of the fly before the sleep phase while the activity
201 of R5 neurons slowly decreases. As with the two-population model (Methods 4.5), the timescale of sleep and wake
202 phases depends on the time constants of the plasticity rules.

203 Once the switching signal reaches the lower threshold, the system switches back to wake phase and the input
204 is turned on again (Figure 4D). Furthermore, if we prevent dFB from switching to the sleep phase (by setting the
205 variable $d(t) = 1$) and thus extend the wake period (sleep deprivation, upper orange region), $w_{EE}^{(16,sum)}$ for wedge
206 neuron 16 crosses the boundary for stability, $w_{EE}^{(16,sum)} > 2$. In this case, the bump in the ring attractor starts to
207 oscillate (Figure 4C; see section 2.5). Towards the end of the extended wake phase, the bump stops tracking the
208 input. In the subsequent sleep phase, more time is required to reset the excitatory weights and to reach the lower
209 threshold $r_I^{(max)}$, resulting in sleep rebound (Figure 4A).

210 2.7 Resetting the ring attractor during sleep using autonomous dynamics

An alternative mechanism for the network to be reset during sleep is an anti-hebbian plasticity rule in $w_{EE}^{(ij)}(t)$, such as the following:

$$\tau_{EE} \dot{w}_{EE}^{(ij)}(t) = -r_E^{(i)}(t)r_E^{(j)}(t) \quad \text{for } i, j = 1, \dots, N. \quad (7)$$

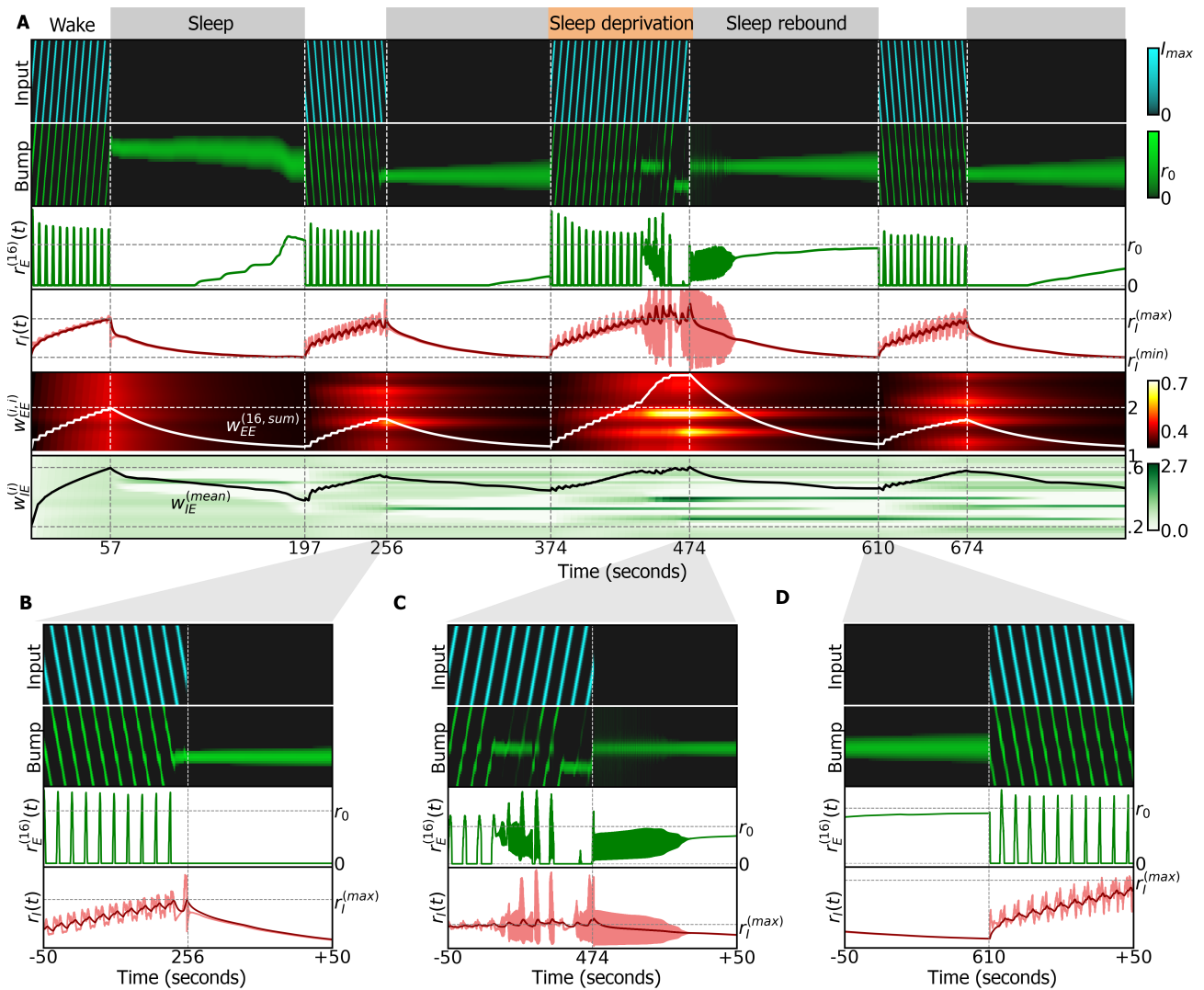


Figure 4. Simulation of ring attractor combined with sleep homeostasis model, using an exponentially decaying plasticity rule during sleep (equation (6)). **A** Entire simulation over a period of 800 seconds. White and grey regions indicate the sleep and wake phases, and correspond to dFB neurons switching off and on, respectively. Top row: input (inhibited during the sleep phase), alternating between clockwise and counter-clockwise rotations at 0.5 Hz. Second row: ring attractor bump activity. Third row: activity of wedge neuron 16. Fourth row, light red: activity of ring neurons. Dark red: filtered activity. Switching between sleep and wake is carried out by dFB neurons that switch on and off depending on filtered activity crossing thresholds $r_I^{(min)}$ and $r_I^{(max)}$. In the third wake epoch, sleep deprivation is produced by extending the inhibition of dFB neurons ($d(t) = 1$ during the orange top layout). Fifth row: diagonal elements of the connectivity matrix $w_{EE}^{(ij)}$. The white line is the sum of all excitatory connections to wedge neuron 16. It passes threshold 2 at around 240 seconds leading to oscillations. The full connectivity matrix $w_{EE}^{(ij)}$ at the switch times is shown in Figure S7. Sixth row: connectivity $w_{IE}^{(i)}$; black line is the mean value. **B** Zoom-in around 256 seconds: switch from wake to sleep phase. **C** Zoom-in around 474 seconds: extended wake phase leads to oscillatory behavior. Circuit switches to sleep. **D** Zoom-in around 610 seconds: switch from sleep to wake phase.

211 This rule produces LTD with correlated activity between neighboring wedge neurons. Figure 5A shows a
 212 simulation of this model. In the wake phase, the behavior is, as expected, the same as in the model without

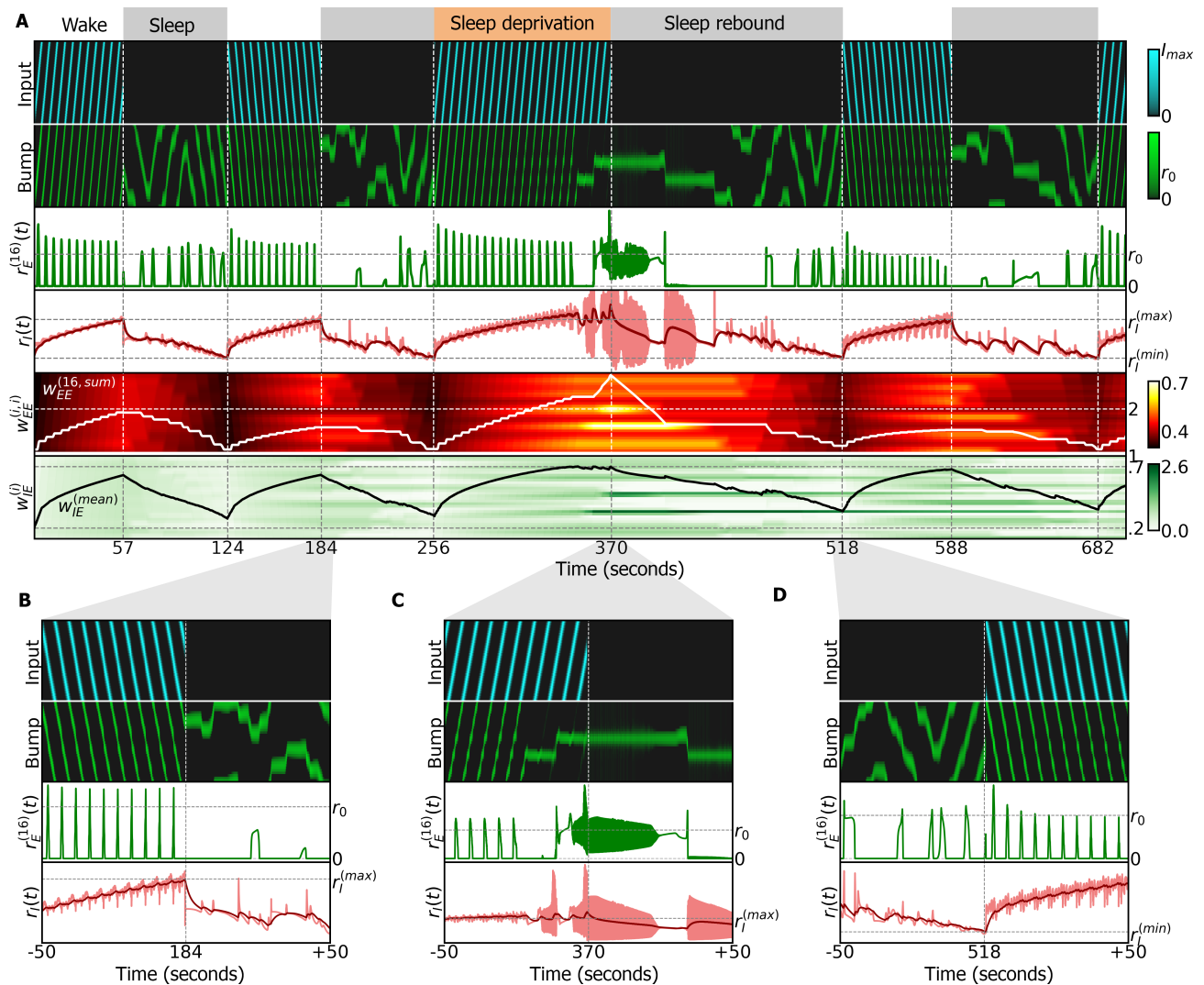


Figure 5. Simulation of ring attractor combined with sleep homeostasis model, using an anti-Hebbian plasticity rule during sleep (equation (7)). **A** Entire simulation over a period of 700 seconds, similar to Figure 4A. **B** Zoom-in around 184 seconds: switch from wake to sleep phase. **C** Zoom-in around 370 seconds: extended wake phase leads to oscillatory behavior. Circuit switches to sleep. **D** Zoom-in around 518 seconds: switch from sleep to wake phase.

213 anti-Hebbian plasticity (Figure 4A). During sleep, the autonomous bump movement resets synaptic connections and
 214 the activity of R5 neurons decreases. Heterogeneity in the weights $w_{EE}^{(ij)}$ (due to synaptic plasticity) makes the bump
 215 drift across wedge neurons. These autonomous dynamics reset the connectivity in the network⁷. The amplitude of
 216 the bump during autonomous dynamics is at setpoint level, that is, below the activity level resulting with input to the
 217 attractor network.

218 Wake phases without continuous input can also show drift (see Figure S8 with intermittent input). This wake
 219 drift is however different from sleep drift, since it ends once the bump reaches the location of strongest recurrent
 220 excitation, making the synaptic weights grow in this location until sleep is initiated. Such wake drift can be reduced
 221 in our model by slowing the plasticity rules and with close to homogeneous coverage of the bump movement across
 222 all wedge neurons (see Figure S9 and Methods (4.9)).

223 To investigate how such autonomous dynamics of the bump during sleep are linked to the dynamics during the
 224 preceding wake phase, we provided sinusoidal inputs a range of amplitudes A and frequencies f . In Figure 6A,

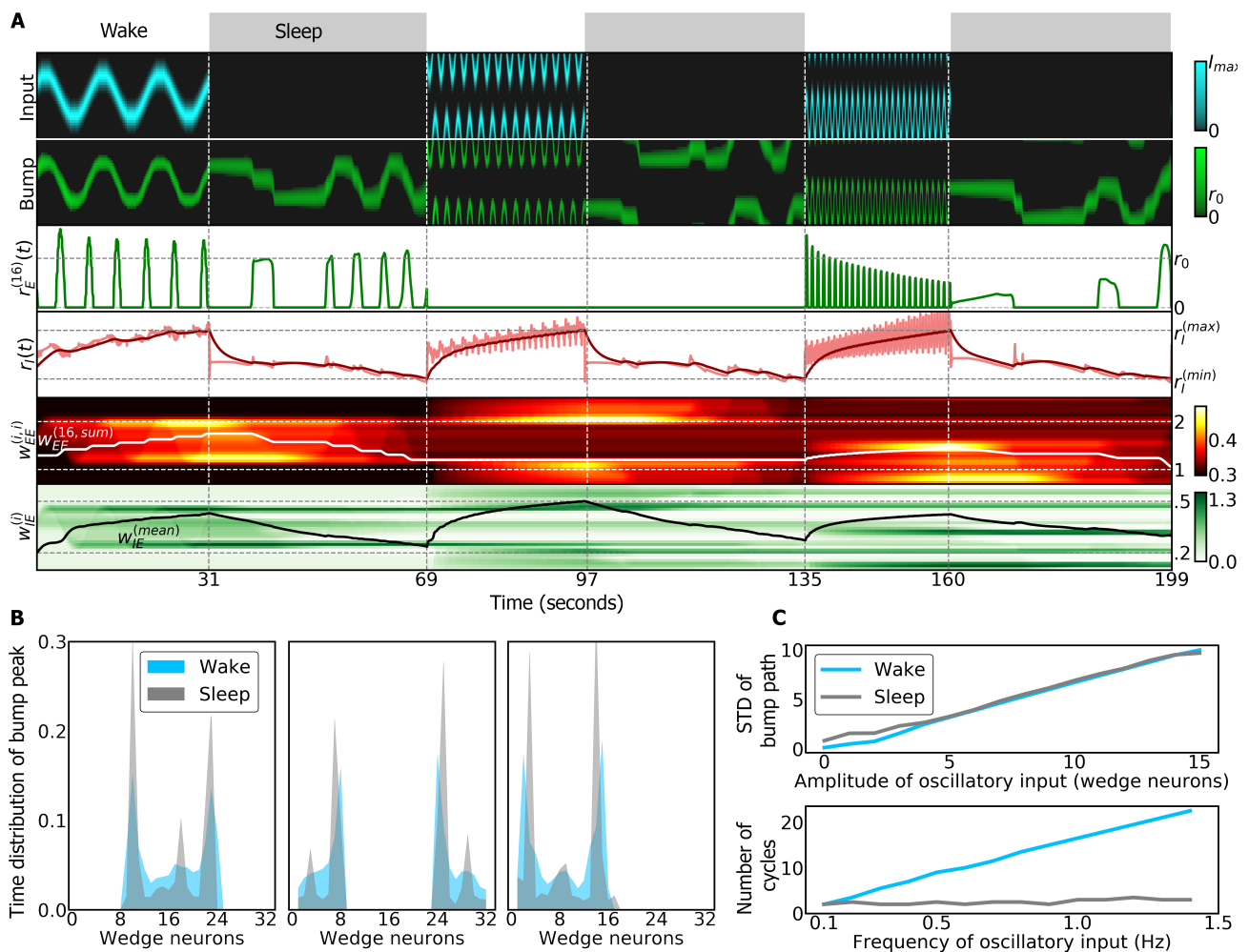


Figure 6. Simulation of the ring attractor network with sinusoidal inputs during wake phase. **A** In each wake phase, a sinusoidal input is provided to the ring attractor (top row) with increasing frequencies in consecutive wake phases. During sleep, an autonomous bump of activity revisits wedge neurons active in the previous wake phase (second row). The third row shows the activity of wedge neuron 16 and the fourth row shows the activity of the ring neuron (light red) and its filtered activity (dark red) used to switch between wake and sleep phases. The last two rows represent the synaptic weights that increase during wakefulness and decrease during sleep. **B** Normalized distribution of time that the bump peak is localized in each wedge neuron during wake (blue) and sleep (grey) phases. The first, second and third plots show the distribution for the first, second and third wake and sleep phases, respectively. **C** Top: standard deviation (STD) of the bump path during a total of 15 simulations where different amplitudes of a sinusoidal inputs are provided during the wake phase. During the wake phase, the STD of the bump path is proportional to the amplitude (grey). During sleep, the autonomous bump path has a correlated STD (Pearson correlation coefficient: 0.99 ($p = 1.5 \cdot 10^{-17}$)). Bottom: number of cycles of the bump path during a total of 15 simulations with different frequencies of a sinusoidal input during wake phase. During the wake phase, the number of cycles is proportional to the input frequency. However, during sleep, the number of cycles does not correlate with the input frequency: Pearson correlation coefficient: 0.76 ($p = 0.0015$).

225 we show a simulation with fixed amplitude, $A = N/4$ and different frequencies in each wake phase (0.1, 0.5, and 1
 226 Hz). During sleep, the bump revisits wedge neurons that were active in the preceding wake phase, as seen in the
 227 distributions of the time spent around each wedge neuron during the first (left), second (center) and third (right)

228 wake phase (in blue) and during the following sleep phase (in grey) (Figure 6B). To further probe the amplitude
229 dependence, we simulated a wake phase and the subsequent sleep phase, and in each simulation varied the amplitude
230 A of a sinusoidal input in the range $[0, 16]$, with fixed frequency of $f = 1\text{Hz}$, during the wake phase. The standard
231 deviation (STD) of the paths of the bump during the wake (blue) and sleep (grey) phase closely match (Figure 6C).
232 Similarly, we investigated the frequency dependence with a stimulus with fixed amplitude, $A = N/4$, and varying
233 frequency in the range $[0.1, 1.5]\text{Hz}$. The number of oscillatory cycles grows linearly with the input frequency in the
234 wake phase (blue), but remains constant during sleep. Therefore, the dynamics during sleep do not depend on the
235 input frequency during the wake phase (Figure 6C). Additionally, the frequency of oscillations of the bump around
236 the ring can increase as the bump approaches the lower threshold of the switching signal (before waking up, Figure
237 S9A). Such autonomous dynamics are reminiscent of activity observed during sleep in mice⁴¹.

238 3 Discussion

239 In the brain of *Drosophila*, structurally similar neurons in the center of the brain have been assigned functionally very
240 different roles. On the one hand, navigation related ring neurons encode spatial memory or visual features^{22,23,42}.
241 For these ring neurons, ring attractor networks offer a compelling structure-function relationship which can provide
242 a rationale for their ring-shaped morphology. On the other hand, sleep related ring neurons serve as homeostatic
243 sleep integrator, encoding sleep drive through structural^{19,28} and activity changes^{19,27}. The connectome additionally
244 shows multiple interactions between these sleep and navigation related circuits^{14,30}.

245 To elucidate the relationship between these navigation and sleep functionalities of ring neurons, and to address
246 how the head direction system can operate in the face of plasticity in connected circuits, we therefore asked what
247 role the homeostatic integrator could play in the ring attractor framework.

248 To address this question, we used the sleep homeostasis model proposed in¹⁸ as a starting point. The connectome
249 shows that this circuit is not isolated but interacts with the head direction system (Figure 2A). When connectivity
250 in this circuit is fixed, however, the increasing activity of R5 neurons (which encode sleep drive) decreases the
251 amplitude of the bump of activity in the ring attractor (Figure 2D). To overcome this problem of vanishing activity, we
252 therefore propose a model with plasticity in R5 neurons (which is experimentally observed) and with hypothesized
253 recurrent plasticity between wedge neurons. In this model (Figure 2C), sleep drive balances plasticity in wedge
254 neurons, which are now able to maintain a bump of activity that evolves towards a constant amplitude setpoint over
255 time. The model also allows variability in the bump amplitude with external (for example visual or self-motion
256 related) input (Figure S4), consistent with experimentally observed behavior-related changes in bump amplitude⁴⁰.

257 However, prolonged activity during wakefulness ultimately leads to unstable behavior (oscillations in Fig. 3C
258 and 5A). Therefore, to restore the connectivity in the head direction system to baseline, we introduced a sleep phase,
259 in agreement with models of sleep homeostasis¹⁸, where the synaptic connections between wedge neurons are reset
260 by LTD. While the time course and dynamics of this reset is not known, we here investigated two alternatives. In
261 one case, while dFB neurons inhibit input, the ring attractor resets to its initial state while the bump stays in place.
262 In the second case, an anti-Hebbian rule resets the ring attractor with autonomous dynamics. These dynamics are
263 linked to the dynamics during wakefulness through their spatial (Figures 6A and 6B) but not through their frequency
264 distributions (Figures 6A and 6C). The amplitude of the bump during autonomous dynamics is at setpoint level, that
265 is, at the level of activity to which the amplitude settles in the absence of (visual or idiothetic) input.

266 In the proposed model, heterogeneities in recurrent connections of wedge neurons can also lead to drift during the
267 wake phase with intermittent inputs (see Figure S8). While this is consistent with the heterogeneities observed in the
268 connectome (Figure S1B), we minimize drift in the model by the slow dynamics of the plasticity rules together with
269 assumed homogeneous activation of wedge neurons over time (S9). Other solutions to avoid drift in ring attractors
270 have however been developed (for example⁴³⁻⁴⁵).

271 Many aspects of this model can also be captured by a simpler two-population model, which shows similar
272 dynamics and related boundaries between the different dynamic regimes (Figures S3B and 3B).

273 The introduction of plasticity was motivated by the observation of structural, synaptic and functional changes in
274 R5 neurons^{19,27,28} as well as their interaction with the head direction system as suggested by the connectome^{14,30,46}.

275 The proposed combined sleep homeostasis and ring attractor model can capture this increase in activity in R5
276 neurons during wakefulness^{19,28} (Figures 6 and 5). Additionally, in the proposed models, sleep deprivation leads
277 to a qualitative change in the behavior of R5 neurons towards oscillatory dynamics which is reminiscent of the
278 experimentally observed transition to bursting dynamics¹⁹ or increase in oscillatory dynamics²⁷. Whether sleep
279 deprivation compromises the head direction system in behaving flies is currently not known, although navigation
280 related memories are for example affected by sleep deprivation in bees^{47,48}.

281 The proposed model makes several predictions that could be tested experimentally. First, we assume LTP in the
282 recurrent connections of wedge neurons during wakefulness (which could also be achieved through an intermediate
283 population³⁴). This plasticity in w_{EE} could be a result of correlated activity between neighboring wedge neurons.
284 Second, as a result of this plasticity, the bump width changes with w_{EE} , decreasing over time spent awake due to LTP
285 in wedge neurons and therefore increasing spatial resolution (and *vice versa* during sleep, Figure S6C). Generally,
286 there is a range of bump widths that can be sustained by the ring attractor (Figure 3). A third model prediction is that
287 extended wakefulness can disrupt the head direction system by producing oscillatory or bursting behavior and will
288 lock the bump position in place (independent of external input, Figure 5A, sleep deprivation). Additionally, sleep
289 results in autonomous dynamics in the ring attractor model (Figure 5), with the network transitioning towards faster
290 dynamics towards the end of the sleep phase (Figure S9). Such autonomous dynamics are reminiscent of activity of
291 the head direction system observed in mice during sleep⁴¹.

292 We further assume that the plasticity rule in the head direction system changes during sleep from LTP to LTD.
293 This change of plasticity has been proposed in several models of sleep (for example⁴⁹; see⁴ for review). A potential
294 mechanism could for example be neuromodulation of an STDP gate^{50,51}, which has been observed in insects^{52,53}
295 and could involve the strong innervation of the central complex by neuromodulatory neurons⁵⁴. For example, ExR1
296 neurons described in¹⁸ (modeled in Figure 1A and B) could produce the switch in plasticity between sleep and wake
297 phases, potentially through neuromodulation (similar to the related serotonergic ExR3 neurons^{30,55}).

298 The resulting weakening of synaptic strength during sleep underlies several hypotheses about sleep function^{4-6,8}.
299 The approach implemented here is based on the idea of reverse learning⁵⁻⁷: during sleep, attractors within the ring
300 attractor network generated during wakefulness are removed and the corresponding increased weights are weakened.
301 Autonomous dynamics during sleep could be functionally relevant for memory consolidation and organization⁵⁶.
302 For instance, flies could partially replay (in wedge neurons) trajectories during sleep that they performed during
303 navigation in the wake phase (see Figure 6A) which could be used by downstream circuits to consolidate navigation
304 related memories. Navigation memories are for example consolidated during sleep in bees⁴⁷, and replay of neural
305 activity in the central complex during sleep has been suggested to consolidate courtship memory in flies⁵⁷.

306 While synaptic changes during sleep and wakefulness are observed across the fly brain (for example⁵⁸), one
307 could hypothesize that such activity related changes are stronger in areas where activity is persistent with a possible
308 role in working memory, such as the head direction system^{25,42}. Therefore, inhibitory R5 neurons might increase
309 their activity faster and require resetting through sleep sooner than other transiently active neurons, ultimately being
310 responsible for signaling sleep drive. We additionally did not differentiate between different ring attractor inputs
311 (for example visual or idiothetic) and such different signals could also be integrated in different ring neurons or
312 homeostats¹¹ (taking for example into account that visual experience increases sleep need⁵⁹).

313 The connectome shows that both the head direction as well as the sleep homeostasis circuits encompass a large
314 number of connected cell types in the central complex^{30,60}. Nevertheless, strongly simplified models of ring attractor
315 networks with only a limited subset of actually involved cell types have proven useful for the description of the head
316 direction system. Similarly, for the sleep homeostasis circuit, many more connected cell types could be considered
317 and we here only investigated a simplified network that nevertheless can capture several experimental observations.

318 Overall, the interaction of the homeostatic integrator and the head direction systems together with mounting
319 evidence for a close structure-function relationship in these circuits, suggest that a relationship between the control
320 and function of sleep could be established in this network using theoretical modeling and experiments.

321 References

- 322 1. Killgore, W. D. Effects of sleep deprivation on cognition. In *Progress in brain research*, vol. 185, 105–129
323 (Elsevier, 2010).
- 324 2. Krause, A. J. *et al.* The sleep-deprived human brain. *Nat. Rev. Neurosci.* **18**, 404 (2017).
- 325 3. Tobaldini, E. *et al.* Sleep, sleep deprivation, autonomic nervous system and cardiovascular diseases. *Neurosci.*
326 *& Biobehav. Rev.* **74**, 321–329 (2017).
- 327 4. Rennó-Costa, C., da Silva, A. C. C., Blanco, W. & Ribeiro, S. Computational models of memory consolidation
328 and long-term synaptic plasticity during sleep. *Neurobiol. learning memory* **160**, 32–47 (2019).
- 329 5. Crick, F. & Mitchison, v. The function of dream sleep. *Nature* **304**, 111–114 (1983).
- 330 6. Hopfield, J. J., Feinstein, D. & Palmer, R. ‘unlearning’ has a stabilizing effect in collective memories. *Nature*
331 **304**, 158–159 (1983).
- 332 7. Thiele, J., Diehl, P. & Cook, M. A wake-sleep algorithm for recurrent, spiking neural networks. *arXiv preprint*
333 *arXiv:1703.06290* (2017).
- 334 8. Tononi, G. & Cirelli, C. Sleep and the price of plasticity: from synaptic and cellular homeostasis to memory
335 consolidation and integration. *Neuron* **81**, 12–34 (2014).
- 336 9. Cirelli, C. & Tononi, G. Linking the need to sleep with synaptic function. *Science* **366**, 189–190 (2019).
- 337 10. Liu, D. & Dan, Y. A motor theory of sleep-wake control: arousal-action circuit. *Annu. review neuroscience*
338 (2019).
- 339 11. Kirszenblat, L. & van Swinderen, B. Sleep in drosophila. In *Handbook of Behavioral Neuroscience*, vol. 30,
340 333–347 (Elsevier, 2019).
- 341 12. Jenett, A. *et al.* A gal4-driver line resource for drosophila neurobiology. *Cell reports* **2**, 991–1001 (2012).
- 342 13. Simpson, J. H. & Looger, L. L. Functional imaging and optogenetics in drosophila. *Genetics* **208**, 1291–1309
343 (2018).
- 344 14. Xu, C. S. *et al.* A connectome of the adult drosophila central brain. *BioRxiv* (2020).
- 345 15. Beckwith, E. J. & French, A. S. Sleep in drosophila and its context. *Front. physiology* **10**, 1167 (2019).
- 346 16. Dubowy, C. & Sehgal, A. Circadian rhythms and sleep in drosophila melanogaster. *Genetics* **205**, 1373–1397
347 (2017).
- 348 17. Donlea, J. M., Alam, M. N. & Szymusiak, R. Neuronal substrates of sleep homeostasis; lessons from flies, rats
349 and mice. *Curr. opinion neurobiology* **44**, 228–235 (2017).
- 350 18. Donlea, J. M. *et al.* Recurrent circuitry for balancing sleep need and sleep. *Neuron* **97**, 378–389 (2018).
- 351 19. Liu, S., Liu, Q., Tabuchi, M. & Wu, M. N. Sleep drive is encoded by neural plastic changes in a dedicated
352 circuit. *Cell* **165**, 1347–1360 (2016).
- 353 20. Donlea, J. M., Pimentel, D. & Miesenböck, G. Neuronal machinery of sleep homeostasis in drosophila. *Neuron*
354 **81**, 860–872 (2014).
- 355 21. Omoto, J. J. *et al.* Neuronal constituents and putative interactions within the drosophila ellipsoid body neuropil.
356 *Front. neural circuits* **12**, 103 (2018).
- 357 22. Ofstad, T. A., Zuker, C. S. & Reiser, M. B. Visual place learning in drosophila melanogaster. *Nature* **474**,
358 204–207 (2011).
- 359 23. Seelig, J. D. & Jayaraman, V. Feature detection and orientation tuning in the drosophila central complex. *Nature*
360 **503**, 262 (2013).
- 361 24. Okubo, T. S., Patella, P., D’Alessandro, I. & Wilson, R. I. A neural network for wind-guided compass navigation.
362 *Neuron* **107**, 924–940 (2020).

- 363 **25.** Seelig, J. D. & Jayaraman, V. Neural dynamics for landmark orientation and angular path integration. *Nature*
364 **521**, 186 (2015).
- 365 **26.** Skaggs, W. E., Knierim, J. J., Kudrimoti, H. S. & McNaughton, B. L. A model of the neural basis of the rat's
366 sense of direction. In *Advances in neural information processing systems*, 173–180 (1995).
- 367 **27.** Raccuglia, D. *et al.* Network-specific synchronization of electrical slow-wave oscillations regulates sleep drive
368 in drosophila. *Curr. Biol.* **29**, 3611–3621 (2019).
- 369 **28.** Huang, S., Piao, C., Beuschel, C. B., Götz, T. & Sigrist, S. J. Presynaptic active zone plasticity encodes sleep
370 need in drosophila. *Curr. Biol.* (2020).
- 371 **29.** Pimentel, D. *et al.* Operation of a homeostatic sleep switch. *Nature* **536**, 333 (2016).
- 372 **30.** Hulse, B. K. *et al.* A connectome of the drosophila central complex reveals network motifs suitable for flexible
373 navigation and context-dependent action selection. *bioRxiv* (2020).
- 374 **31.** Franconville, R., Beron, C. & Jayaraman, V. Building a functional connectome of the drosophila central
375 complex. *Elife* **7**, e37017 (2018).
- 376 **32.** Kim, S. S., Rouault, H., Druckmann, S. & Jayaraman, V. Ring attractor dynamics in the drosophila central brain.
377 *Science* **356**, 849–853 (2017).
- 378 **33.** Hulse, B. K. & Jayaraman, V. Mechanisms underlying the neural computation of head direction. *Annu. Rev.*
379 *Neurosci.* **43** (2019).
- 380 **34.** Green, J. & Maimon, G. Building a heading signal from anatomically defined neuron types in the drosophila
381 central complex. *Curr. opinion neurobiology* **52**, 156–164 (2018).
- 382 **35.** Hanesch, U., Fischbach, K.-F. & Heisenberg, M. Neuronal architecture of the central complex in drosophila
383 melanogaster. *Cell Tissue Res.* **257**, 343–366 (1989).
- 384 **36.** Lin, C.-Y. *et al.* A comprehensive wiring diagram of the protocerebral bridge for visual information processing
385 in the drosophila brain. *Cell reports* **3**, 1739–1753 (2013).
- 386 **37.** Wolff, T., Iyer, N. A. & Rubin, G. M. Neuroarchitecture and neuroanatomy of the drosophila central complex:
387 A gal4-based dissection of protocerebral bridge neurons and circuits. *J. Comp. Neurol.* **523**, 997–1037 (2015).
- 388 **38.** Faville, R., Kottler, B., Goodhill, G., Shaw, P. & Van Swinderen, B. How deeply does your mutant sleep?
389 probing arousal to better understand sleep defects in drosophila. *Sci. reports* **5**, 8454 (2015).
- 390 **39.** Gerstner, W. & Kistler, W. M. Mathematical formulations of hebbian learning. *Biol. cybernetics* **87**, 404–415
391 (2002).
- 392 **40.** Dana, H. *et al.* High-performance calcium sensors for imaging activity in neuronal populations and microcom-
393 partments. *Nat. Methods* **16**, 649–657 (2019).
- 394 **41.** Peyrache, A., Lacroix, M. M., Petersen, P. C. & Buzsáki, G. Internally organized mechanisms of the head
395 direction sense. *Nat. neuroscience* **18**, 569–575 (2015).
- 396 **42.** Neuser, K., Triphan, T., Mronz, M., Poeck, B. & Strauss, R. Analysis of a spatial orientation memory in
397 drosophila. *Nature* **453**, 1244–1247 (2008).
- 398 **43.** Renart, A., Song, P. & Wang, X.-J. Robust spatial working memory through homeostatic synaptic scaling in
399 heterogeneous cortical networks. *Neuron* **38**, 473–485 (2003).
- 400 **44.** Itskov, V., Hansel, D. & Tsodyks, M. Short-term facilitation may stabilize parametric working memory trace.
401 *Front. computational neuroscience* **5**, 40 (2011).
- 402 **45.** Seeholzer, A., Deger, M. & Gerstner, W. Stability of working memory in continuous attractor networks under
403 the control of short-term plasticity. *PLoS computational biology* **15**, e1006928 (2019).
- 404 **46.** Turner-Evans, D. B. *et al.* The neuroanatomical ultrastructure and function of a biological ring attractor. *bioRxiv*
405 847152 (2019).

- 406 **47.** Beyaert, L., Greggers, U. & Menzel, R. Honeybees consolidate navigation memory during sleep. *J. Exp. Biol.*
407 **215**, 3981–3988 (2012).
- 408 **48.** Vorster, A. P. & Born, J. Sleep and memory in mammals, birds and invertebrates. *Neurosci. & Biobehav. Rev.*
409 **50**, 103–119 (2015).
- 410 **49.** Nere, A. T., Hashmi, A., Cirelli, C. & Tononi, G. Sleep-dependent synaptic down-selection (i): modeling the
411 benefits of sleep on memory consolidation and integration. *Front. neurology* **4**, 143 (2013).
- 412 **50.** Brzosko, Z., Mierau, S. B. & Paulsen, O. Neuromodulation of spike-timing-dependent plasticity: past, present,
413 and future. *Neuron* **103**, 563–581 (2019).
- 414 **51.** Pawlak, V., Wickens, J. R., Kirkwood, A. & Kerr, J. N. Timing is not everything: neuromodulation opens the
415 stdp gate. *Front. synaptic neuroscience* **2**, 146 (2010).
- 416 **52.** Cassenaer, S. & Laurent, G. Conditional modulation of spike-timing-dependent plasticity for olfactory learning.
417 *Nature* **482**, 47–52 (2012).
- 418 **53.** Feldman, D. E. The spike-timing dependence of plasticity. *Neuron* **75**, 556–571 (2012).
- 419 **54.** Kahsai, L. & Winther, Å. M. Chemical neuroanatomy of the drosophila central complex: distribution of multiple
420 neuropeptides in relation to neurotransmitters. *J. Comp. Neurol.* **519**, 290–315 (2011).
- 421 **55.** Liu, C. *et al.* A serotonin-modulated circuit controls sleep architecture to regulate cognitive function independent
422 of total sleep in drosophila. *Curr. Biol.* **29**, 3635–3646 (2019).
- 423 **56.** Sejnowski, T. J. Neural networks: Sleep and memory. *Curr. Biol.* **5**, 832–834 (1995).
- 424 **57.** Dag, U. *et al.* Neuronal reactivation during post-learning sleep consolidates long-term memory in drosophila.
425 *ELife* **8**, e42786 (2019).
- 426 **58.** Bushey, D., Tononi, G. & Cirelli, C. Sleep and synaptic homeostasis: structural evidence in drosophila. *Science*
427 **332**, 1576–1581 (2011).
- 428 **59.** Kirszenblat, L., Yaun, R. & van Swinderen, B. Visual experience drives sleep need in drosophila. *Sleep* (2019).
- 429 **60.** Shiozaki, H. M., Ohta, K. & Kazama, H. A multi-regional network encoding heading and steering maneuvers in
430 drosophila. *Neuron* (2020).
- 431 **61.** Saper, C. B., Chou, T. C. & Scammell, T. E. The sleep switch: hypothalamic control of sleep and wakefulness.
432 *Trends neurosciences* **24**, 726–731 (2001).
- 433 **62.** Behn, C. G. D., Brown, E. N., Scammell, T. E. & Kopell, N. J. Mathematical model of network dynamics
434 governing mouse sleep–wake behavior. *J. neurophysiology* **97**, 3828–3840 (2007).
- 435 **63.** Rempe, M. J., Best, J. & Terman, D. A mathematical model of the sleep/wake cycle. *J. mathematical biology*
436 **60**, 615–644 (2010).
- 437 **64.** Dunmyre, J. R., Mashour, G. A. & Booth, V. Coupled flip-flop model for rem sleep regulation in the rat. *PLoS*
438 *One* **9**, e94481 (2014).
- 439 **65.** Borbély, A. A. A two process model of sleep regulation. *Hum neurobiol* **1**, 195–204 (1982).
- 440 **66.** Dayan, P. & Abbott, L. F. Theoretical neuroscience: computational and mathematical modeling of neural
441 systems. (2001).
- 442 **67.** Kim, S. S., Hermundstad, A. M., Romani, S., Abbott, L. & Jayaraman, V. Generation of stable heading
443 representations in diverse visual scenes. *Nature* **576**, 126–131 (2019).
- 444 **68.** Fisher, Y. E., Lu, J., D’Alessandro, I. & Wilson, R. I. Sensorimotor experience remaps visual input to a
445 heading-direction network. *Nature* **576**, 121–125 (2019).

446 Funding

447 Max Planck Society, Center of Advanced European Studies and Research. P.J.G was supported by the German
448 Research Foundation (DFG) through SFB 1089 ‘Synaptic Microcircuits’.

449 Acknowledgements

450 We would like to thank Raoul-Martin Memmesheimer for helpful discussions and comments on the manuscript, and
451 Gerry Rubin, Julijana Gjorgjieva, Felipe Kalle Kossio, and Marina Elaine Wosniack for helpful discussions.

452 Disclosures

453 The authors declare that there are no conflicts of interest related to this article.

454 4 Methods

455 4.1 Anatomy based on the fly connectome

456 The connectivity of the proposed model is based on the fly connectome¹⁴ and incorporates the populations R5 (ER5),
457 ExR1, EPG and EL, as described in the Neuprint database. Each population and its innervation in the ellipsoid body
458 are shown in Figure S1A. EL and EPG neurons, respectively, have diagonal connectivity matrices within and across
459 populations as shown in Figure S1B.

460 4.2 Numerical simulation of models

461 We numerically solved all models with forward Euler with a time step of $dt = 0.0001$ seconds. Our code is
462 implemented in Python, and we will make it available upon publication.

463 4.3 Sleep homeostasis circuit

In this and the following, we use rate-based models to simulate dynamics of entire neural populations and dynamics
of single wedge neurons. The differential equations used to model the sleep homeostasis circuit are as follows:

$$\begin{cases} \tau_I \dot{r}_I(t) = -r_I(t) + [r_H(t)]_+ \\ \tau \dot{r}_{ExR1}(t) = -r_{ExR1}(t) + [1 - r_{dFB}(t)]_+ \\ \tau \dot{r}_{dFB}(t) = -r_{dFB}(t) + [G(r_I) - d(t)]_+ \end{cases} \quad (8)$$

464

The switch behavior of dFB neurons is modeled by simple hysteresis, according to the following equation:

$$G(r_I) = \begin{cases} 1 & \text{if } r_I(t) < r_I^{(max)} \text{ and } \dot{r}_I(t) > 0 \\ 0 & \text{if } r_I(t) \geq r_I^{(max)} \text{ and } \dot{r}_I(t) > 0 \\ 0 & \text{if } r_I(t) > r_I^{(min)} \text{ and } \dot{r}_I(t) < 0 \\ 1 & \text{if } r_I(t) \leq r_I^{(min)} \text{ and } \dot{r}_I(t) < 0 \end{cases} \quad (9)$$

465

466 Such a switch behavior in dFB neurons could be implemented, for example, by adding an additional wake-
467 promoting population, which together with dFB neurons, could mutually inhibit each other to create a flip-flop
468 switch, similar to sleep models proposed in mammals^{61–64}. Candidates for the wake-promoting population in the fly
469 are dopaminergic neurons in the PPM3 and PPL1 clusters²⁹. Alternatively, this switch behavior could be generated
470 by a single-cell mechanism in dFB neurons, which are known to increase excitability with extended wake time²⁹.

In this model, the wake and sleep time depend on the effective time constant τ_I and the thresholds $r_I^{(min)}$ and
 $r_I^{(max)}$. The time spent in the sleep phase, t_S (sleep time) as a function of the time spent in the wake phase, t_W (wake

time), can be computed by solving the differential equation for R5 neurons, r_I , during the sleep phase and wake phase, respectively:

$$t_S(t_W) = \tau_I \log\left(\frac{1 + (r_I^{(min)} - 1)e^{-t_W/\tau_I}}{r_I^{(min)}}\right) \quad (10)$$

471

Considering that t_W is small, we can expand this expression in a Taylor series, taking only first order terms:

$$t_S \approx \frac{1 - r_I^{(min)}}{r_I^{(min)}} t_W \quad (11)$$

472

For small waking time periods, the sleep time t_S increases linearly, resulting in sleep rebound as required for homeostasis (increased time spent awake leads to more sleep afterwards). However, for long wake times, the preceding sleep time saturates at a constant value t_S^{sat} , given by the following expression:

$$t_S^{sat} = \tau_I \log\left(\frac{1}{r_I^{(min)}}\right) \quad (12)$$

473

474 This saturation time prevents very large sleep times after large preceding wake times, and it is also a feature
475 observed experimentally⁶⁵.

476 4.4 Sleep homeostasis and ring attractor with fixed connections

We asked how increasing activity in R5 neurons affects the head direction circuit in the absence of plasticity. Given the fact that R5 and wedge neurons are connected, we modeled a ring attractor network where wedge neurons encode head direction and R5 neurons provide increasing inhibitory input to wedge neurons. The model is shown schematically in Figure 2A and described by the following system of equations:

$$\begin{cases} \tau \dot{r}_E^{(i)}(t) = -r_E^{(i)}(t) + \left[\sum_j^N w_{EE}^{(ij)} r_E^{(j)}(t) - w_{EI} r_I + \theta + I^{(i)}(m, t) \right]_+ & \text{for } i = 1, \dots, N \\ \tau_I \dot{r}_I(t) = -r_I(t) + \left[\sum_j^N w_{IE}^{(j)} r_E^{(j)}(t) + w_{IH} r_H(t) \right]_+, \end{cases} \quad (13)$$

477 where $r_E(t)^{(i)}$ represents the activity of a wedge neuron i (in total, $N = 32$) and $r_I(t)$ is the population activity
478 of R5 neurons and τ_I accounts for slow dynamics as in the phenomenological sleep homeostasis model (section
479 2.1). We only model the wake phase for simplicity, where dFB neurons are assumed to have zero activity and
480 activity in ExR1 neurons is defined as $r_H(t) = 1$, similar to the sleep homeostasis model. We neglect the connection
481 from wedge to ExR1 neurons for simplicity, since we focus on the interaction between wedge and R5 neurons.
482 The weights w_{AB} represent the connectivity from population B to population A . The recurrent connectivity $w_{EE}^{(ij)}$ is
483 a matrix, in which for a given presynaptic wedge neuron, i , the element (ij) is given by a gaussian function that
484 depends on the distance to the postsynaptic wedge neuron j along the ring, given by equation (38) (see for example
485 Figure 3C, left top). In this model, the values of the synaptic weights w_{IE} and w_{IH} were chosen such that the activity
486 of ring neurons increases¹⁹.

477 Figure 2B shows a simulation of the model, where a rotating input $I(m, t)$ is provided to wedge neurons at 0.5
488 Hz (top row, blue). The activity of R5 neurons increases, as imposed by our parameter choice (third row, red). The
489 wedge neurons, (second row, green) follow the rotating input while receiving this increasing inhibition, such that the
490 bump amplitude decreases over time until inhibition gets strong enough so that the bump vanishes.

491 4.5 Two-population model with plasticity for R5 and wedge neurons

To simplify the analysis and build intuitions about the complete ring attractor model combined with the sleep homeostasis circuit, we first developed a simpler model. This model is a population model based on an excitatory-inhibitory network⁶⁶ (Figure S3A) and describes the interaction between wedge and R5 neurons. The dynamics of

(excitatory) wedge and (inhibitory) ring neurons are described by the following system of differential equations:

$$\begin{cases} \tau \dot{r}_E(t) = -r_E(t) + \left[w_{EE}(t)r_E(t) - w_{EI}r_I(t) + \theta \right]_+ \\ \tau \dot{r}_I(t) = -r_I(t) + \left[w_{IE}(t)r_E(t) \right]_+, \end{cases} \quad (14)$$

492 where $r_E(t)$ and $r_I(t)$ are the firing rates at time t of wedge neurons and ring neurons, respectively, w_{AB} is the
493 synaptic weight from population B to population A , θ is a constant background input onto wedge neurons, $[\cdot]_+$ is a
494 threshold-linear function to ensure positive-valued firing rates, and τ is the effective population time constant.

495 4.5.1 Plasticity rules

We additionally introduce plasticity rules for the excitatory weights w_{EE} and w_{IE} during the wake phase (which we motivate below):

$$\begin{cases} \tau_{EE} \dot{w}_{EE}(t) = r_E(t)r_E(t) \\ \tau_{IE} \dot{w}_{IE}(t) = r_I(t)r_E(t)(r_E(t) - r_0), \end{cases} \quad (15)$$

496 During the sleep phase we change the plasticity rule in w_{EE} , while leaving unchanged the plasticity rule in w_{IE} :

$$\begin{cases} \tau_{EE} \dot{w}_{EE}(t) = -r_E(t)r_E(t) \\ \tau_{IE} \dot{w}_{IE}(t) = r_I(t)r_E(t)(r_E(t) - r_0), \end{cases} \quad (16)$$

where τ_{EE} and τ_{IE} are time constants, and r_0 is a positive presynaptic threshold. While the first plasticity rule is a linear Hebbian rule, the second is a triplet rule with presynaptic threshold. These plasticity rules can be extracted from a general form of Hebbian plasticity. A general hebbian plasticity rule for a synaptic weight w_{ij} can be defined as follows:

$$\tau_{ij} \dot{w}_{ij} = F(w_{ij}, r_i, r_j), \quad (17)$$

where τ_{ij} is the time constant of the rule, and $F(\cdot)$ is a function that depends on the synaptic weight, w_{ij} , and on pre- and postsynaptic activities, r_j and r_i , respectively³⁹. The function $F(\cdot)$ needs to fulfill Hebb's condition: to produce a change in the synaptic weight w_{ij} , the pre- and postsynaptic neurons must be active: $r_i > 0$, $r_j > 0$. In principle, this function is unknown, but we can expand it in a Taylor series³⁹ around $r_I = r_E = 0$:

$$\tau_{ij} \dot{w}_{ij} \approx c_{00} + c_{10}r_i + c_{11}r_j + c_{20}r_i^2 + c_{21}r_i r_j + c_{22}r_j^2 + c_{30}r_i^3 + c_{31}r_i^2 r_j + c_{32}r_i r_j^2 + c_{33}r_j^3 + O(r^4), \quad (18)$$

497 where each coefficient depends on the connection strength $c_{mn} = c_{mn}(w_{ij})$. The values of these coefficients determine
498 the plasticity rule. For instance, Hebbian plasticity rules that are linear in the neural activities can be obtained
499 by setting second or higher order coefficients to zero³⁹. Keeping higher order coefficients leads to rules with
500 non-linearities.

We assume that the plasticity rule in $w_{EE}(t)$ during the wake phase is linear, obtained by setting $c_{21} = 1$ and all other coefficients to zero, while the plasticity rule in w_{IE} is non linear on the presynaptic neural activity, obtained by setting $c_{21} = -r_0$, $c_{32} = 1$ and the other coefficients to zero (equation (16)). To ensure that synapses remain excitatory or inhibitory throughout the system's dynamics at any time, the plasticity rules are threshold-rectified at zero if the synaptic weights are zero:

$$\begin{cases} \dot{w}_{EE}(t) = \left[\dot{w}_{EE}(t) \right]_+ & \text{if } w_{EE}(t) = 0 \\ \dot{w}_{IE}(t) = \left[\dot{w}_{IE}(t) \right]_+ & \text{if } w_{IE}(t) = 0. \end{cases} \quad (19)$$

501 These plasticity rules are motivated by the fact that R5 neurons produce sleep drive by increasing activity and
502 synaptic strength¹⁹ for balancing LTP in wedge neurons. The plasticity rules in equation (16) produce the following

τ	τ_f	τ_{EE}	τ_{IE}	w_{EI}	θ	r_0	$r_I^{(min)}$	$r_I^{(max)}$
0.01	2	10000	10000	0.5	10	10	20	35

Table S1. Parameter values used in the two-population model. Time constants τ , τ_f , τ_{EE} and τ_{IE} are measured in seconds. We consider the rest dimensionless quantities.

503 effects: (i) The synaptic connection between wedge neurons, w_{EE} and between wedge and ring neurons, w_{IE} , get
 504 stronger during the wake phase. (ii) The firing rate of ring neurons r_I increases during the wake phase. (iii) The
 505 firing rate of the entire population of wedge neurons evolves always to a constant setpoint, $r_E \rightarrow r_0$.

506 Finally, we note that the dynamics of the plasticity rules are much slower than the dynamics of neural populations,
 507 so that $\tau_{EE}, \tau_{IE} \gg \tau$. The parameters for the two-population model used for simulations are shown in Table S1, but
 508 the following stability analysis is performed without any assumption on the parameter values.

509 4.5.2 Stability of the two-population model

Fast-timescale limit In the fast-timescale limit, we can assume that $\tau_{EE}, \tau_{IE} \rightarrow \infty$, meaning that synaptic plasticity is sufficiently slow compared to the dynamics of the neural populations so that it can be assumed to be constant. This offers the advantage of treating the synaptic weight w_{EE} as a free parameter with a fixed value, assuming that w_{IE} has already evolved through its plasticity rule to its equilibrium value, $r_E \rightarrow r_0$. Therefore, for a given value of w_{EE} , we set the value of w_{EI} such that the fixed point for the wedge neurons is r_0 . In this way, the value of w_{IE} is coupled to the value of w_{EE} . The stability of the 2-dimensional system given by equations in (14) is then analyzed with respect to the value of w_{EE} . Since the system is piecewise linear due to the threshold function $[\cdot]_+$, we perform a linear analysis assuming that the inputs to the neurons are positive. Under these conditions, the fixed point of the system, (r_E^*, r_I^*) , is given by the following expressions:

$$\begin{cases} r_E^* = w_{EE}r_E^* - w_{EI}r_I^* + \theta = r_0 \\ r_I^* = w_{IE}r_0. \end{cases} \quad (20)$$

Since we force the fixed point of wedge neurons to be r_0 , we can extract the equilibrium value of w_{IE} as a function of w_{EE} :

$$w_{IE} = \frac{\theta}{w_{EI}r_0} + \frac{w_{EE} - 1}{w_{EI}}. \quad (21)$$

The fixed point of the system can be described with respect to w_{EE} as:

$$\begin{cases} r_E^* = r_0 \\ r_I^* = \frac{\theta}{w_{EI}} + r_0 \frac{w_{EE} - 1}{w_{EI}} \end{cases} \quad (22)$$

Both the fixed point of ring neuron activity, r_I^* , and the equilibrium value of the connectivity, w_{IE} , depend linearly on w_{EE} , implying that if w_{EE} increases, both w_{IE} and r_I^* increase as well as long as the fixed point is stable. We analyze the stability of the system by calculating the eigenvalues:

$$\lambda_{\pm} = \frac{1}{2\tau} \left((w_{EE} - 2) \pm \sqrt{(w_{EE} - 2)^2 - \frac{4\theta}{r_0}} \right). \quad (23)$$

Both eigenvalues are shown in Figure S2A with respect to different values of w_{EE} . This leads to four different cases:

$$\begin{cases} (1) & w_{EE} \in \left[1, 2 - 2\sqrt{\theta/r_0} \right] \\ (2) & w_{EE} \in \left(2 - 2\sqrt{\theta/r_0}, 2 \right] \\ (3) & w_{EE} \in \left(2, 2 + 2\sqrt{\theta/r_0} \right] \\ (4) & w_{EE} > 2 + 2\sqrt{\theta/r_0} \end{cases} \quad (24)$$

510 In case (1), both eigenvalues are real and negative: the fixed point is stable (equation (22)). In case (2), the real
 511 part of the eigenvalues is negative and the imaginary part is non-zero: the system evolves towards the fixed point
 512 with damped oscillations. In case (3), the real part of the eigenvalues is positive and the imaginary part is non-zero:
 513 the system diverges towards infinity, oscillating with amplitudes which increase exponentially. In case (4), the
 514 eigenvalues are real and positive: the fixed point is unstable. This analysis predicts a bifurcation in the stability of
 515 the fixed point when $w_{EE} = 2$. This behavior is shown in Figure S3C.

516 The non-linearity of the linear threshold function changes the behavior of the model slightly. While the behavior
 517 stays the same for the cases (1), (2) and (4), because the model is mostly in the linear regime, case (3) differs and the
 518 non-linearity produces stable cycles around the fixed point. This behavior is found empirically from simulating the
 519 non-linear model, and is summarized in Figure S3B.

Slow-timescale limit In the slow-timescale limit we consider that the firing rates change sufficiently fast compared with the synaptic weights so that these changes can be considered instantaneous ($\tau \rightarrow 0$). We therefore analyze the conditions under which the synaptic rules in equations (15) and (16) stabilize the model. We again first consider the linear range of the function $[\cdot]_+$ where the inputs to the neurons are positive. We approximate the instantaneous value of the firing rates in equation (14) as follows:

$$\begin{cases} r_E = w_{EE}(t)r_E - w_{EI}r_I + \theta \\ r_I = w_{IE}(t)r_E \end{cases} \quad (25)$$

This linear system allows extracting the values of r_E and r_I in terms of the synaptic weights as:

$$\begin{cases} r_E = \frac{\theta}{1 - w_{EE} + w_{EI}w_{IE}} \\ r_I = \frac{w_{IE}\theta}{1 - w_{EE} + w_{EI}w_{IE}} \end{cases} \quad (26)$$

We can now compute the vector field for wedge and ring neuron activity as a consequence of the slow dynamics of synaptic plasticity:

$$\begin{cases} \dot{r}_E = \frac{\partial r_E}{\partial w_{EE}} \dot{w}_{EE} + \frac{\partial r_E}{\partial w_{IE}} \dot{w}_{IE} \\ \dot{r}_I = \frac{\partial r_I}{\partial w_{EE}} \dot{w}_{EE} + \frac{\partial r_I}{\partial w_{IE}} \dot{w}_{IE} \end{cases} \quad (27)$$

520 4.5.3 Two-population dynamics during wakefulness

Considering the plasticity rules during the wake phase (15), equation (27) leads to the following system of differential equations:

$$\begin{cases} \dot{r}_E = \frac{w_{EI}r_I \tau_{EE} - \tau_{IE} r_E^3}{\tau_{EE} \tau_{IE}} \frac{r_E^3}{\theta} \left(-r_E + \left(1 + \frac{\tau_{IE}}{w_{EI}r_I \tau_{EE} - \tau_{IE}} \right) r_0 \right) \\ \dot{r}_I = \frac{r_I^3 r_E}{\theta} \left(\frac{1}{\tau_{EE}} + \frac{1 - w_{EE}}{\tau_{IE}} (r_E - r_0) \right) \end{cases} \quad (28)$$

The second equation gives the dynamics of ring neurons, which increase activity with $1/\tau_{EE}$. The first equation gives the dynamics of the population of wedge neurons approaching a setpoint only when the effective decay time constant (the first factor in the right hand side) is positive, otherwise the equation diverges to infinity and the system is unstable. This gives the following criterion for τ_{EE} and τ_{IE} :

$$\frac{\tau_{EE}}{\tau_{IE}} > \frac{1}{w_{EI}r_I} \quad (29)$$

This relationship supports the idea that plasticity in w_{IE} has to be fast enough with respect to the LTP in w_{EE} ; otherwise, if w_{EE} increases faster than w_{IE} , the model diverges. Let us compute the upper limit of inequality (29), which corresponds to the minimum of r_I . For that, we approximate the firing rate of wedge neurons by $r_E = r_0$, and

$r_I = w_{IE}r_0$. Then, we can write w_{IE} as a function of w_{EE} as in equation (21). The upper limit of inequality (29) will therefore happen at the minimum of w_{EE} . As the minimum is $w_{EE} = 1$, the upper limit of the stability condition is:

$$\frac{\tau_{EE}}{\tau_{IE}} > \frac{1}{\theta}. \quad (30)$$

When this condition holds, the setpoint of wedge neurons in equation (28), which is not r_0 as approximated previously, is given by

$$r_E^* = \left(1 + \frac{1}{w_{EI}r_I \frac{\tau_{EE}}{\tau_{IE}} - 1}\right)r_0, \quad (31)$$

521 which is generally different from r_0 due to the inertia of the dynamics of w_{EE} . In the limit $\tau_{EE} \rightarrow \infty$ (no plasticity
522 in w_{EE}), the fixed point is r_0 , as expected from the fast-timescale analysis.

523 Figure S2B shows the vector field for the system of equations (28). The green line shows the trajectory of the
524 setpoint in wedge neurons as the activity of ring neurons increase. As r_I increases due to increasing w_{EE} , the setpoint
525 in r_E approaches r_0 .

526 During wakefulness, the fixed point for wedge neurons r_E^* remains mostly constant, and the fixed point for ring
527 neurons r_I^* changes with w_{EE} (Figure S3B). If $w_{EE} \leq 2$ (light green region), the fixed point (r_E^*, r_I^*) is stable, and both
528 neural populations evolve towards these values. With increasing w_{EE} , the fixed point of ring neurons r_I^* also increases
529 while the fixed point of wedge neurons r_E^* remains constant. If w_{EE} increases further to $2 < w_{EE} \leq 2(1 + \sqrt{\theta/r_0})$,
530 the model enters a regime of stable oscillations (light orange region of Figure S3B). In this regime, both neural
531 populations oscillate around the fixed point with a frequency that changes with w_{EE} (see Figure S2A, as explained
532 in the fast-timescale limit. In addition, ring neurons increase their amplitude of oscillations as w_{EE} increases.
533 Finally, when $w_{EE} \geq 2(1 + \sqrt{\theta/r_0})$ (light red region), the fixed point is unstable and the activity of both populations
534 diverges.

535 Figure S3C illustrates the dynamics of the full system, i.e. the activity of wedge and ring neurons, $r_E(t)$ and
536 $r_I(t)$, as well as synaptic weights, $w_{EE}(t)$ and $w_{IE}(t)$. In the beginning (light green region), the fixed point of ring
537 and wedge neurons is stable because $w_{EE} < 2$. When this boundary is crossed, the system enters the regime of
538 stable oscillations (light orange region). Also, in the stable region of the simulation in Figure S3C, w_{EE} , w_{IE} and
539 ring neuron activity r_I increase, while the activity of wedge neurons r_E remains constant as imposed by conditions
540 (i)-(iii). w_{EE} , w_{IE} and r_I constitute therefore a measure of how far the network has moved from its initial state.

541 4.5.4 Two-population model dynamics during sleep

542 In order to reset the system back to its stable state ($w_{EE} < 2$) after prolonged activity (wakefulness), we introduce
543 a sleep phase with inverted plasticity⁵⁻⁷. For this we assume that during sleep the recurrent connection between
544 wedge neurons, w_{EE} , gets weaker through LTD^{4,7} while the plasticity rule for w_{IE} is the same as in the wake phase
545 (equation (16)).

We can perform the same analysis during sleep by considering the plasticity rule in equation (16) during sleep so
that the equations (27) lead to the following system of differential equations:

$$\begin{cases} \dot{r}_E = \frac{w_{EI}r_I \tau_{EE} + \tau_{IE}}{\tau_{EE} \tau_{IE}} \frac{r_E^3}{\theta} \left(-r_E + \left(1 - \frac{\tau_{IE}}{w_{EI}r_I \tau_{EE} + \tau_{IE}}\right)r_0 \right) \\ \dot{r}_I = \frac{r_I^3 r_E}{\theta} \left(-\frac{1}{\tau_{EE}} + \frac{1-w_{EE}}{\tau_{IE}} (r_E - r_0) \right). \end{cases} \quad (32)$$

The second equation shows how ring neurons decrease their activity with $1/\tau_{EE}$, at the same rate as in the
wake phase. The first equation shows a fixed point for wedge neurons that is lower than r_0 , due to the inertia of a
decreasing w_{EE} during sleep, given by:

$$r_E^* = \left(1 - \frac{1}{w_{EI}r_I \frac{\tau_{EE}}{\tau_{IE}} + 1}\right)r_0. \quad (33)$$

546 Figure S2C shows the vector field given by equation (32) during the sleep phase, where the trajectory of the
 547 setpoint of wedge neurons (the green line) diverges from r_0 as the activity of ring neurons decreases.

The impact of LTD on the model during sleep can be understood by inspecting Figure S3B: with decreasing value of w_{EE} , the fixed points become stable (light green) and the activity of ring neurons decreases (as shown in the fast-timescale limit). The switch between the wake and sleep phases is performed by dFB neurons that sense activity of R5 neurons¹⁹. Since R5 and dFB are not anatomically but functionally connected¹⁹, we apply a low-pass filter to the activities of R5 neurons, which act as an input to dFB neurons and remove possible oscillations. We refer to this filtered activity as the switching signal, and it is modeled, together with dFB neurons as follows:

$$\begin{cases} \tau_f \dot{r}_I^{(f)}(t) = -r_I^{(f)}(t) + r_I(t) \\ \tau \dot{r}_S(t) = -r_S(t) + [G(r_I^{(f)}(t)) - d(t)]_+ \end{cases} \quad (34)$$

548 where τ_f is the time constant of the low-pass filter $r_I^{(f)}$ and $r_S(t)$ is the activity of dFB neurons with a switching
 549 behavior modeled by equation (9). The variable $d(t)$ is a variable intended to produce sleep deprivation.

550 Figure S3D shows a simulation of the model combining subsequent wake (white regions), where dFB neurons
 551 are inactive, and sleep phases (grey), where dFB are active. During wakefulness, w_{EE} and w_{IE} undergo LTP and
 552 the activity of R5 neurons increases (light red line in second row in Figure S3D) and r_E is constant. When the
 553 switching signal (dark red line in second row) crosses an upper threshold, $r_I^{(max)}$, dFB neurons switch the model to
 554 sleep. During sleep, w_{EE} undergoes LTD due to the switch in plasticity, while the activity of R5 neurons decreases.
 555 w_{IE} also undergoes LTD (note that the plasticity rule does not change) since it follows the trend of w_{EE} to impose
 556 the set-point r_0 to the wedge neurons.

557 Therefore, sleep resets synaptic plasticity and activity of R5 neurons. Once the switching signal reaches a
 558 lower threshold, $r_I^{(min)}$, the model is switched back to the wake phase. In the third wake phase, we simulated sleep
 559 deprivation by setting $d(t) = 1$ (top orange region). Here, w_{EE} crosses the bifurcation boundary, $w_{EE} > 2$, and the
 560 model enters the domain of stable oscillations.

561 During the following sleep phase, the system needs more time to fully reset and reach the lower threshold. Such
 562 sleep rebound after sleep deprivation is an experimentally described feature of sleep homeostasis circuits^{17,18}.

563 The time that the system spends in the sleep and wake phases is determined by the time constants of the plasticity
 564 rules, τ_{EE} and τ_{IE} , and the upper and lower thresholds of the switching signal, $r_I^{(min)}$ and $r_I^{(max)}$. In our simulations,
 565 we set τ_{EE} and τ_{IE} to yield dynamics in the timescale of seconds (for ease of visualization), but larger values lead to
 566 similar behavior on longer timescales (minutes or hours, see Figure S8).

567 4.6 Ring attractor network with plasticity

We expand the two-population model to a ring attractor network. A total of $N = 32$ individual wedge neurons are modeled by $r_E^{(i)}(t)$. For simplicity, ring neurons are modeled as a population, $r_I(t)$. The model is schematically shown in Figure 2D. The dynamics of the ring attractor network are given by the following equations:

$$\begin{cases} \tau \dot{r}_E^{(i)}(t) = -r_E^{(i)}(t) + \left[\sum_j^N w_{EE}^{(ij)}(t) r_E^{(j)}(t) - w_{EI} r_I(t) + \theta + I^{(i)}(m) \right]_+ & \text{for } i = 1, \dots, N \\ \tau \dot{r}_I(t) = -r_I(t) + \left[\sum_j^N w_{IE}^{(j)}(t) r_E^{(j)}(t) \right]_+ \end{cases} \quad (35)$$

The synaptic plasticity rules are also extended from the two-population model during the wake phase:

$$\begin{cases} \tau_{EE} \dot{w}_{EE}^{(ij)}(t) = r_E^{(i)}(t) r_E^{(j)}(t) & \text{for } i, j = 1, \dots, N \\ \tau_{IE} \dot{w}_{IE}^{(i)}(t) = r_I(t) r_E^{(i)}(t) (r_E^{(i)}(t) - r_0) & \text{for } i = 1, \dots, N, \end{cases} \quad (36)$$

and during the sleep phase:

$$\begin{cases} \tau_{EE} \dot{w}_{EE}^{(ij)}(t) = -r_E^{(i)}(t) r_E^{(j)}(t) & \text{for } i, j = 1, \dots, N \\ \tau_{IE} \dot{w}_{IE}^{(i)}(t) = r_I(t) r_E^{(i)}(t) (r_E^{(i)}(t) - r_0) & \text{for } i = 1, \dots, N. \end{cases} \quad (37)$$

τ	τ_f	τ_{EE}	τ_{IE}	w_{EI}	θ	r_0	$r_I^{(min)}$	$r_I^{(max)}$	$w_{EE}^{(max)}$	σ	I_{max}	I_σ
0.01	2	10000	10000	0.5	10	10	22	30	0.3	1.5	5	2

Table S2. Parameter values used in the ring attractor network. As in the previous model, time constants τ , τ_f , τ_{EE} and τ_{IE} are measured in seconds. We consider the rest dimensionless quantities.

We initialize the synaptic weights $w_{EE}^{(ij)}$ with a Gaussian function with amplitude $w_{EE}^{(max)}$ and standard deviation σ :

$$w_{EE}^{(ij)} = w_{EE}^{(max)} \exp\left(-\frac{\left(\min[|i-j|, N-|i-j|]\right)^2}{2\sigma^2}\right). \quad (38)$$

Additionally we provide a Gaussian input to the ring attractor around a given wedge neuron m with amplitude I_{max} and standard deviation I_σ :

$$I^{(i)}(m, t) = I_{max} \left[\exp\left(-\frac{\left(\min[|i-m(t)|, N-|i-m(t)|]\right)^2}{2I_\sigma^2}\right) - r_S(t) \right]. \quad (39)$$

568 This input allows changing the position of the bump in the simulations, and can represent visual or idiothetic
569 input to update the head direction of the animal.

570 We use the low-pass filtered activity of ring neurons to switch between sleep and wake phases, as in equation (5).
571 The values of the parameters in Table S2 are used in all simulations unless stated otherwise.

572 Synaptic plasticity in ring and wedge neurons has been discussed in several studies^{19,27,28,67,68}. Note that we
573 here focus on plasticity in the connections from wedge to ring neurons, while leaving the connectivity in the opposite
574 direction constant. This is opposite from^{67,68}, where plasticity from ring to wedge neurons is assumed, while the
575 other direction is left constant. This choice is motivated by the increasing activity in R5 neurons during the wake
576 phase¹⁹, which could be explained by the growth of dendritic synaptic sites (pre-synaptic plasticity), for instance
577 from wedge to R5 neurons – consistent with the data and interpretation in¹⁹ –, but not by the growth of axonal
578 synaptic sites (post-synaptic plasticity).

579 4.7 Ring attractor network: bump stability analysis

To analyze to stability of the ring attractor model, we use an approach similar to the one in the fast-timescales
analysis of the two-population model. First, we assume no plasticity in the recurrent connections $w_{EE}^{(ij)}$ but only in
 $w_{IE}^{(ij)}$,

$$\begin{cases} \tau_{EE} \dot{w}_{EE}^{(ij)}(t) = 0 \\ \tau_{IE} \dot{w}_{IE}^{(i)}(t) = r_I(t) r_E^{(i)}(t) (r_E^{(i)}(t) - r_0) \end{cases} \quad \text{for } i = 1, \dots, N. \quad (40)$$

We analyze the stability and behavior of the network while gradually changing $w_{EE}^{(ij)}$. We initialize the ring
attractor network with a bump profile, where neuron number 16 has maximum activity $r_E^{(16)} > r_E^{(j)}, \forall j \neq 16$. Given
that only the connections $w_{IE}^{(i)}$ are plastic, the activity of ring neurons converges to a stable value given by

$$r_I \longrightarrow w_{IE}^{(16)} r_0. \quad (41)$$

580 This can be understood by looking at the plasticity rule for $w_{IE}^{(i)}$ (40). First, all the synaptic weights evolve so that
581 wedge neuron 16 approaches the activity r_0 . As all wedge neurons receive the same global inhibition, and wedge
582 neuron 16 has maximum activity, the activity of the other wedge neurons is lower than r_0 . At this point, the weights

583 $w_{IE}^{(k)}$ for wedge neurons $k \neq 16$ with non-zero activity, decrease over time until reaching zero. On the other hand, if
 584 a wedge neuron $q \neq 16$ has zero activity, it does not provide any input to the ring neurons. As for wedge neuron
 585 16, the synaptic plasticity rule changes the value of $w_{IE}^{(16)}$ such that its activity approaches r_0 . An example of this
 586 behavior can be seen in Figure S5A, where we initialize the system with an input such that the peak of the bump
 587 is at wedge neuron 16. The synaptic weights $w_{IE}^{(k)}$ for wedge neurons $k \neq 16$ which have non-zero activity evolve
 588 towards zero.

589 The value of $w_{IE}^{(16)}$ is determined by the bump profile, because $r_E^{(16)}$ is receiving input from any wedge neuron
 590 with non-zero activity. Thus $w_{IE}^{(16)}$ has to balance the total excitation to set the activity of the wedge neuron 16 to r_0 .
 591 Furthermore, the bump profile is determined by the parameters of the recurrent connectivity profile $w_{EE}^{(ij)}$, i.e. $w_{EE}^{(max)}$
 592 and σ (equation (38)). If we fix the amplitude $w_{EE}^{(max)}$ and increase the standard deviation σ , the width of the bump,
 593 that is the number of active wedge neurons, decreases. This is because more wedge neurons are providing input
 594 to wedge neuron 16 as σ increases, and the value of $w_{IE}^{(16)}$ increases to set $r_E^{(16)} = r_0$, which in turn provides more
 595 inhibition through ring neurons to all the wedge neurons and lowers their activities, reducing at the same time the
 596 bump width. This behavior is seen in Figure S5A and S5B.

597 The bump also shows oscillatory behavior (Figure S5C) depending on the value of σ . In general, the state of
 598 the ring attractor network and its stability can be described in terms of the recurrent connectivity distribution, $w_{EE}^{(ij)}$,
 599 consistent with the fast-timescale limit analysis in the two-population model.

To investigate how the behavior and stability of the ring attractor network depend on the recurrent connections
 $w_{EE}^{(ij)}$, we simulated the ring attractor model for a grid of values for the parameters $w_{EE}^{(max)}$ and σ :

$$\left\{ \begin{array}{ll} w_{EE}^{(max)} \in [0.1, 0.6) & \text{with step } 0.005 \\ \sigma \in [1, 6) & \text{with step } 0.05. \end{array} \right. \quad (42)$$

600 In total, we performed 10000 simulations where we initialize the bump peak in wedge neuron 16 with a
 601 predefined input of 0.5 seconds, and let the network evolve for 10 seconds. We then analyzed the stability and
 602 behavior of the system in the last second of each simulation, therefore assuming that the state of the network does
 603 not change. Figure S5 shows an example of 3 simulations with different σ values; the light orange band across all
 604 simulations highlights the region used for analysis.

605 In this region we computed for each simulation the following:

- 606 • **Oscillation frequency:** the frequency at which wedge neuron 16 oscillates. For this, we computed the
 607 Discrete Fourier Transform, and the resulting peak value corresponds to the oscillation frequency.
- 608 • **Mean bump FWHM:** the mean value over time of the full width at half maximum of the bump, a proxy for
 609 the width of the bump.
- 610 • **Maximum bump peak:** the maximum value of the wedge neuron 16 over time.
- 611 • **Mean bump peak:** the mean value over time of the wedge neuron 16. If the bump does not oscillate, this
 612 value is equivalent to the maximum bump peak value.
- 613 • **Mean ring neuron activity:** the mean of ring neuron activity over time.

614 These measures are displayed in Figure S6B, S6C, S6D, S6E and S6F, as a function of the recurrent connectivity
 615 parameters $w_{EE}^{(max)}$ and σ . Figure S6B shows how the network starts oscillating with increasing $w_{EE}^{(max)}$ and σ . On the
 616 other hand, the FWHM in Figure S6B and S6C shows how at low $w_{EE}^{(max)}$ and σ values, the bump disappears and all
 617 wedge neurons have constant activity at r_0 . As the parameter values increase, a bump of activity appears and the
 618 FWHM decreases, as observed in Figure 3C and S5A and B. Finally, the activity of ring neurons increases as $w_{EE}^{(max)}$
 619 and σ increase.

We further characterise the behavior and stability of the bump in the network with the total excitatory connectivity to the wedge neuron with maximal activity, i.e. wedge neuron 16, $w_{EE}^{(16,sum)}$:

$$w_{EE}^{(16,sum)} = \sum_j^N w_{EE}^{(16,j)}. \quad (43)$$

620 Figure S6A highlights the isolines where $w_{EE}^{(16,sum)}$ is constant for different values of $w_{EE}^{(max)}$ and σ . Note how
 621 the constant values of $w_{EE}^{(16,sum)} = 2$ and $w_{EE}^{(16,sum)} = 2(1 + \sqrt{\theta/r_0})$ coincide with the boundaries of the different
 622 dynamic regimes. Therefore, the quantity $w_{EE}^{(16,sum)}$ has in the ring attractor model a similar role as does the
 623 recurrent connection w_{EE} in the two-population model. For $w_{EE}^{(16,sum)} < 1$, the bump disappears, similar to the
 624 two-population network model when $w_{EE} < 1$. However, unlike in the two-population model, which is unstable for
 625 $w_{EE} > 2(1 + \sqrt{\theta/r_0})$, in the ring attractor network, for $w_{EE}^{(16,sum)} > 2(1 + \sqrt{\theta/r_0})$ the wedge neurons are strongly
 626 inhibited by high activity in ring neurons.

From the above analysis we extracted regions of stability that are shown in Figure 3B. Constant lines of $w_{EE}^{(16,sum)}$ are computed as follows: in the continuous limit, i.e. $N \rightarrow \infty$, the total excitatory connectivity is given by the following integral:

$$w_{EE}^{(16,sum)} = \int w_{EE}^{(max)} e^{-\frac{x^2}{2\sigma^2}} dx = w_{EE}^{(max)} \sigma \sqrt{2\pi}. \quad (44)$$

Therefore, the isolines of constant $w_{EE}^{(16,sum)}$ are given by $w_{EE}^{(max)} = w_{EE}^{(16,sum)} / \sigma \sqrt{2\pi}$. For the discrete case, we empirically found $w_{EE}^{(16,sum)}$ to be well approximated by:

$$w_{EE}^{(max)} = \frac{w_{EE}^{(16,sum)}}{C\sigma}, \quad (45)$$

627 for any constant line $w_{EE}^{(16,sum)}$, where $C \approx 2.697$.

628 4.8 Ring attractor network: autonomous bump path analysis

To simulate how the bump in the ring attractor changes position to update the head direction during the wake phase, we use a simple clockwise or counter-clockwise rotating input with frequency f defined by:

$$m(t) = \pm f N t. \quad (46)$$

$m(t)$ is the wedge neuron where the ring attractor receives the Gaussian input $I^{(i)}(m(t))$ (equation (39)), and it is a cyclic variable, so that:

$$\begin{cases} \text{if } m(t) = N + 1 & \longrightarrow m(t) = 1 \\ \text{if } m(t) = 0 & \longrightarrow m(t) = N. \end{cases} \quad (47)$$

During the sleep phase, the bump in the ring attractor shows autonomous dynamics (Figure 5A). To investigate the relationship between the path of the bump during sleep and in the preceding wake phase, we use a sinusoidal input during the wake phase, defined by the amplitude A , frequency f , and the center C :

$$m(t) = C + A \sin(2\pi f t). \quad (48)$$

An example of this input with different frequencies f and centers C is shown in Figure 6A. We can obtain the position of the bump during wake and sleep phases as:

$$P_{bump}(t) = \operatorname{argmax}_i \left[r_E^{(i)}(t) \right], \quad (49)$$

so that the position of the bump corresponds to the wedge neuron with maximum activity. We can now compute the distribution of times that the bump is localized around each wedge neuron i during sleep and wake phases, respectively, as:

$$\begin{cases} t_{wake}^{(i)} = \int_{wake} \delta(P_{bump}(t) - i) dt \\ t_{sleep}^{(i)} = \int_{sleep} \delta(P_{bump}(t) - i) dt, \end{cases} \quad (50)$$

where $\delta(\cdot)$ is the Dirac delta function and integrals extend over the wake and sleep phases. Figure 6B shows these distributions normalized for the three wake phases in Figure 6A and their following sleep phases. The distributions are very similar, meaning that during the sleep phase, the bump revisits the same wedge neurons that were active during the wake phase.

We further asked how the autonomous bump path changes during sleep with respect to the amplitude of the sine-shaped input, A , and frequency, f , during sleep. We first fixed the frequency of the input at $f = 1Hz$ and the center at $C = 16$ while varying the amplitude in the range of $[0, 15]$ with an increment of 1. This resulted in 15 simulations where we computed the standard deviation of the bump path during sleep and wake:

$$\begin{cases} STD_{wake} = \sqrt{\frac{1}{T_{wake}} \int_{wake} (P_{bump}(t) - 16)^2 dt} \\ STD_{sleep} = \sqrt{\frac{1}{T_{sleep}} \int_{sleep} (P_{bump}(t) - 16)^2 dt}, \end{cases} \quad (51)$$

where T_{wake} and T_{sleep} are the duration of wake and sleep phases, respectively. Figure 6C shows the standard deviation in both phases with respect to the amplitude A . Note the similarity between both phases.

Secondly, we fixed the value of the amplitude at $A = 8$ and the center at $C = 16$ while varying the frequency, f , in the range $[0.1, 1.5]$ at increments of $0.1Hz$, resulting in 15 simulations. We quantify the number of cycles during both the sleep and wake phase. During the wake phase, the number of cycles is proportional to the input frequency f . Therefore a linear relationship between the number of cycles during sleep and the frequency of the input would give correlation between the frequency and the autonomously rotating bump path. However, Figure 6C, bottom, shows how the number of cycles during sleep does not change as the input frequency increases. An example of this can be seen in Figure 6A where we increase the frequency in consecutive wake phases and the path of the bump during sleep does not increase the rotation frequency.

4.9 Ring attractor network: bump drift during wake phase

In the simulations and analyses above, we provided input during the wake phase and the ring attractor network closely followed the input with a bump of activity. However, a ring attractor network should be able to sustain the bump of activity in the absence of input. It is known that small changes in the synaptic connections of wedge neurons $w_{EE}^{(ij)}$ can cause drifts of the bump in the absence of input⁴³⁻⁴⁵.

To test for drift during the wake phase, we used a flashing rotating input that turns on and off. The input around a wedge neuron m is on for 0.2 sec (equation (39)), and then is turned off for 0.3 sec. Therefore, for N neurons the rotating input frequency is $1/(0.5N)$. Figure S8A shows such a simulation with three wake and sleep phases and S8B, C and D show zoom-ins around different times. Note how the bump drifts from the provided visual input, due to the synaptic changes in $w_{EE}^{(ij)}$.

This drift depends on the plasticity time constants. For instance, Figure S9 shows a simulation with 100 times larger time constants, $\tau_{EE}, \tau_{IE} = 10^6$. The duration of wake and sleep phases are now in the order of hours, compared to the simulation in Figure S9. Note in the zoom-ins of Figures S9B, C and D that the bump of activity is sustained during the off time of the visual input without drifting. Since there are many more rotations during the wake phase and the synaptic changes in $w_{EE}^{(ij)}$ are very small in each rotation, the weights increase all together very homogeneously.

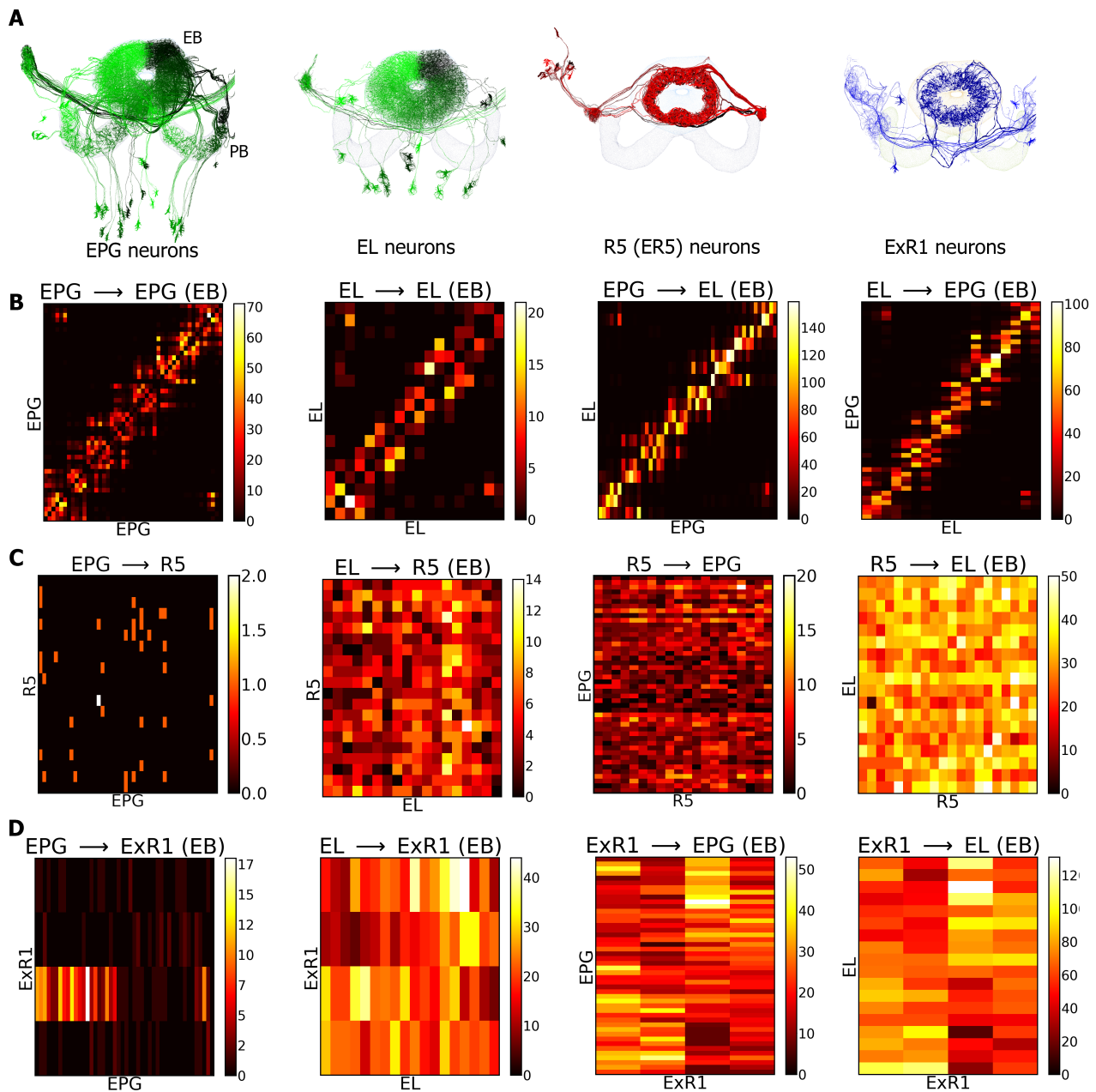


Figure S1. Connectivity between the navigation-related populations (EPG and EL) and sleep-related populations (R5 and ExR1). **A** On the left, neural projections of EPG and EL, referred as wedge neurons (green). On the right, neural projections of R5 (red) and ExR1 (blue). **B** Recurrent connectivity between wedge neurons. The matrix in each figure represents the number of synaptic sites between presynaptic neurons (horizontal axis) and postsynaptic neurons (vertical axis)¹⁴. **C** Connectivity between wedge neurons and R5 neurons in both directions. **D** Connectivity between wedge neurons and ExR1 neurons in both directions. Data and neurons are reproduced from¹⁴.

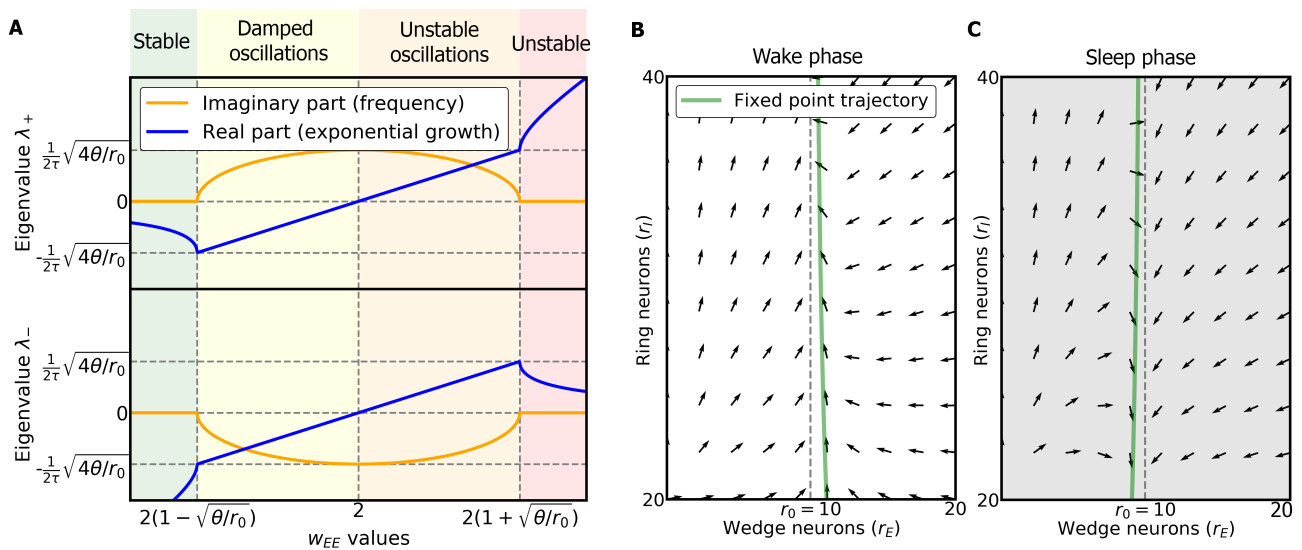


Figure S2. Analysis of the two population model in the fast and slow-timescale limits. **A** Eigenvalues in the two-population model in the fast-timescales limit. The real (in blue) and imaginary (in orange) parts of the eigenvalues are plotted as a function of w_{EE} . **B** Vector field of wedge and ring neurons dependent on synaptic plasticity during the wake phase in the slow-timescale limit. The green line represents the set point trajectory of wedge neurons. **C** Vector field of wedge and ring neurons due to plasticity in the sleep phase in the slow-timescale limit. The green line is the trajectory of the set point in wedge neurons.

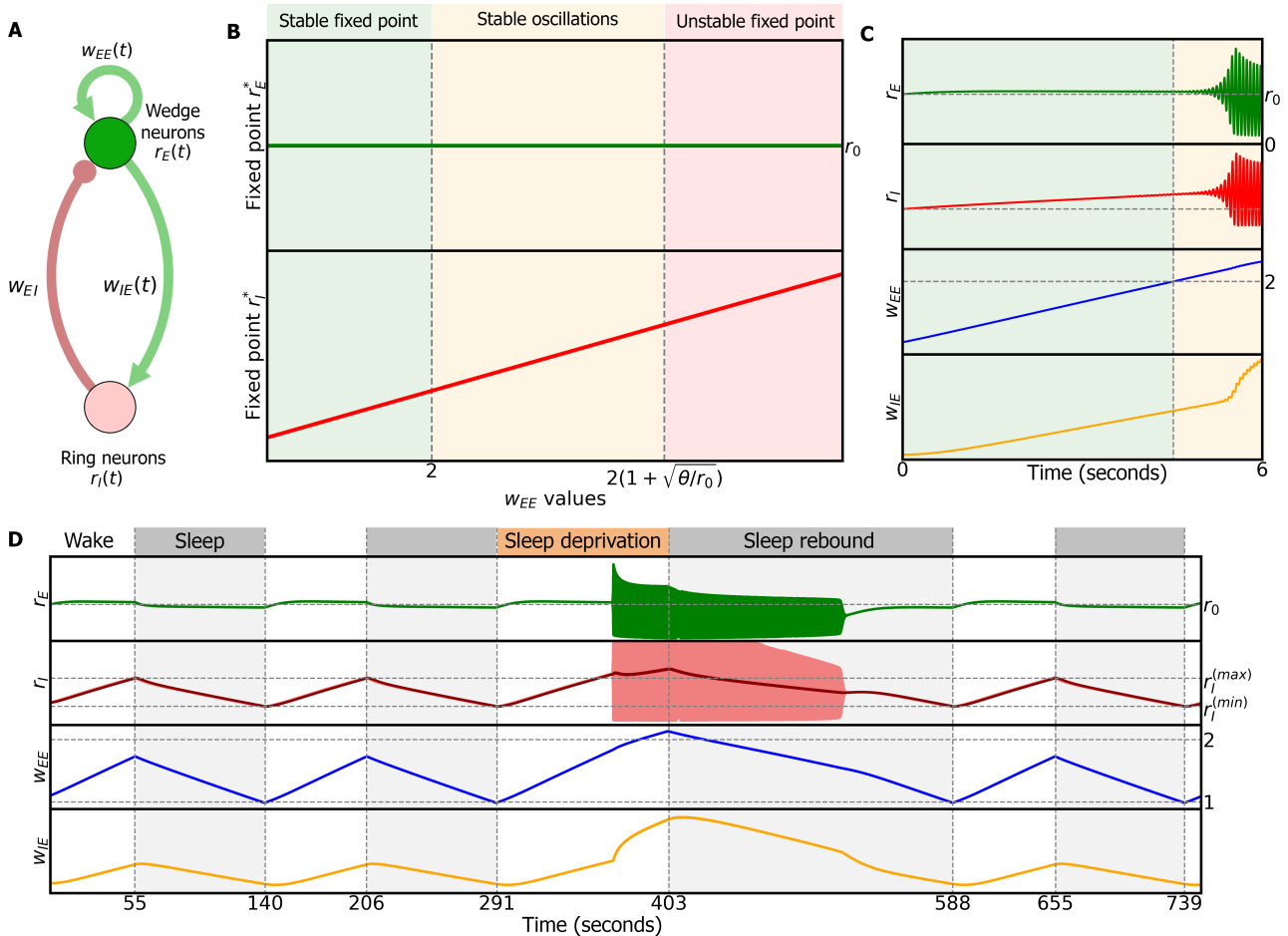


Figure S3. Two-population model. **A** Model describing the dynamics of the activities of excitatory wedge neurons and inhibitory ring neurons, r_E and r_I respectively, and the plasticity of the synaptic weights within the wedge population w_{EE} and from the wedge population to the ring population w_{IE} . Green connections are excitatory, red connections inhibitory. **B** Stability conditions with respect to w_{EE} (fast-timescale limit, see Methods). **C** Dynamics during wake phase. As w_{EE} grows, the system undergoes a Hopf bifurcation (a critical point where the system starts to oscillate) and both populations start to oscillate around a fixed point. **D** Dynamics with alternating sleep and wake phases. Wake phase produces LTP in w_{EE} and w_{IE} and increases the activity of ring neurons. Sleep produces LTD and reduces the activity of ring neurons. Extending the wake period produces sleep deprivation and results in stable oscillations. The subsequently required sleep period for resetting is longer (sleep rebound).

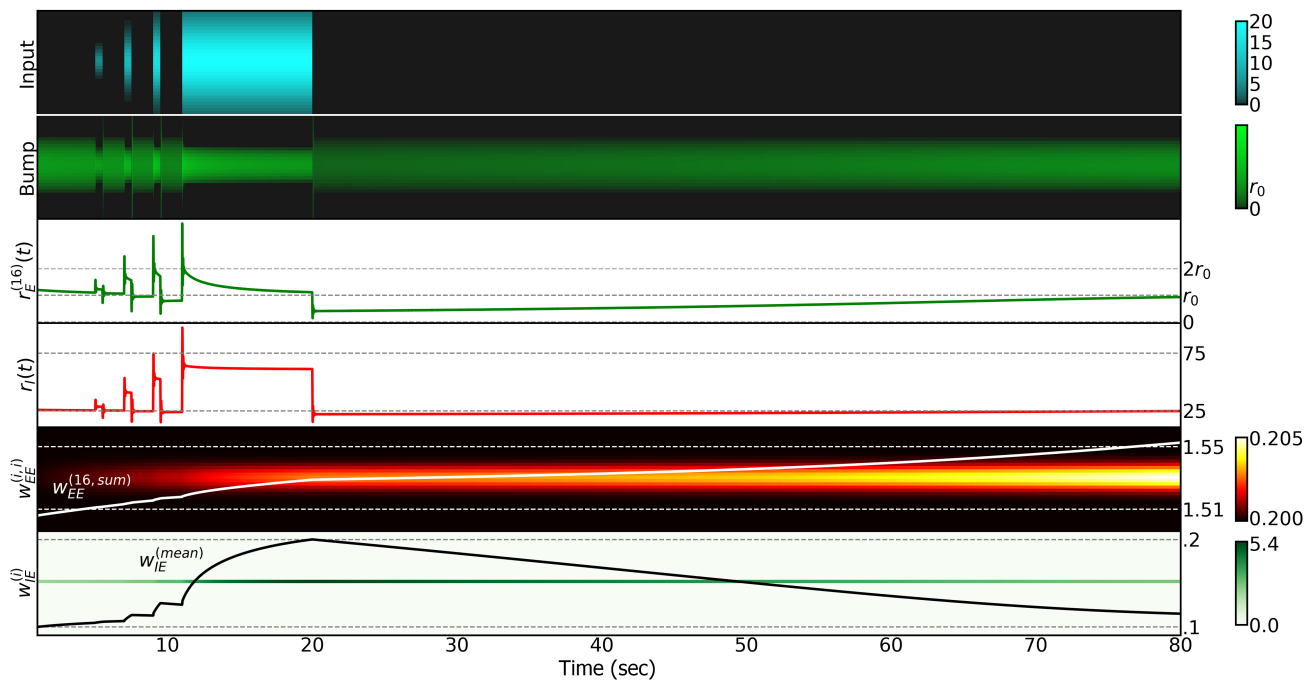


Figure S4. Bump profile in the ring attractor network in response to inputs of different amplitudes I_{max} and standard deviations I_{σ} . When input (first row) is provided to the ring attractor the plasticity rule for $w_{IE}^{(i)}$ brings the activity of the wedge neuron $r_E^{(16)}$ (where the bump peak is located, second row) back to r_0 (third row). The bump is not constrained to have constant activity (third row), but always relaxes towards r_0 over time in the absence of changing input. For ease of visualization, we used a slower time constant for the plasticity of $w_{EE}^{(ij)}$ ($\tau_{EE} = 1000000$), thus avoiding oscillations in the bump throughout the simulation.

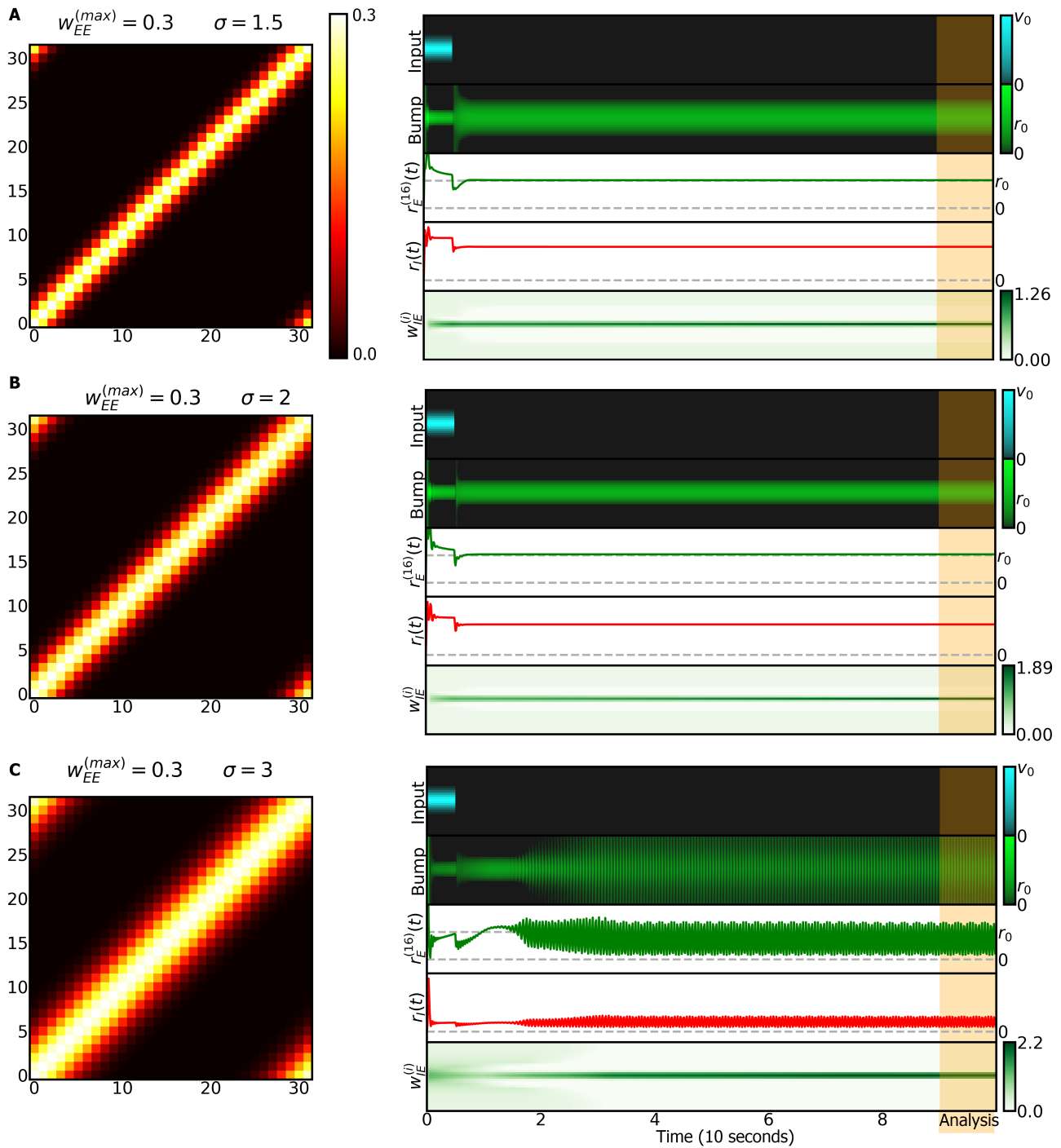


Figure S5. Ring attractor network with no plasticity in $w_{EE}^{(ij)}$ and different initial distributions of weights. **A** Left: initial $w_{EE}^{(ij)}$ values; right: 10 seconds of simulated dynamics. First row: input positioning the bump around wedge neuron 16. Second row: bump profile over time. Third row: activity of wedge neuron 16 evolving towards r_0 due to plasticity in $w_{IE}^{(i)}$. Fourth row: activity of ring neurons. Fifth row: the synaptic weights $w_{IE}^{(i)}$. The orange band at the end of the simulations represents the period in which the stability of the bump is analyzed. **B** Same as A but with larger σ . **C** Same as A, B but again increasing σ . In this simulation, the bump shows stable oscillations.

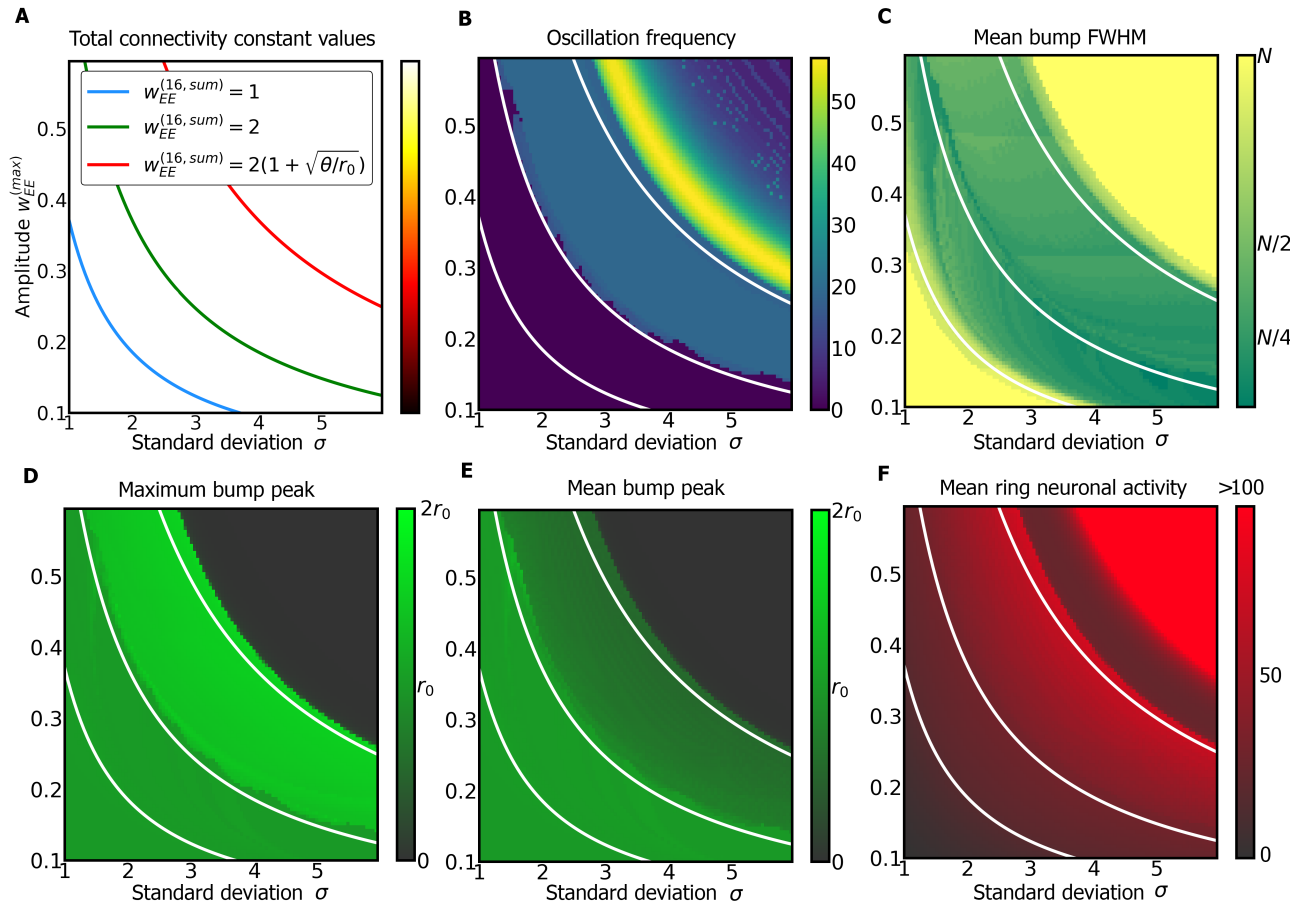


Figure S6. Stability analysis of the bump in the ring attractor network. All subfigures are plots of different measures as a function of the grid of values of σ and $w_{EE}^{(max)}$ that define the fixed synaptic weights $w_{EE}^{(ij)}$ in the bump stability analysis (Methods (4.7)). All variables in B, C, D, E, and F are calculated in a time slot of 1 sec at the end of each simulation (orange area in Figure S3). **A** Isolines of $w_{EE}^{(16,sum)}$. These isolines are overlaid in white in the other subfigures and represent approximate boundaries of stability. **B** Frequency of the oscillations in the bump across the analysis time slot. Above the isline $w_{EE}^{(16,sum)} = 2$, the bump oscillates. **C** Mean FWHM over the analysis time slot. Below the isline $w_{EE}^{(16,sum)} = 1$ and above the isline $w_{EE}^{(16,sum)} = 2(1 + \sqrt{\theta/r_0})$ there is no bump because the FWHM is equal to the number of neurons, N . **D** Maximum peak of the bump in the analysis time slot (maximum activity of wedge neuron 16, $\max(r_E^{(16)}(t))$). Below the isline $w_{EE}^{(16,sum)} = 2$, the maximum is r_0 as forced by the plasticity rule in $w_{IE}^{(i)}$. Between the isolines $w_{EE}^{(16,sum)} = 2$ and $w_{EE}^{(16,sum)} = 2(1 + \sqrt{\theta/r_0})$, the bump oscillates and the amplitude is given by the maximum, in this case $2r_0$. Above $w_{EE}^{(16,sum)} = 2(1 + \sqrt{\theta/r_0})$, there is close-to-zero activity in wedge neurons, since the maximum is near zero. **E** Mean of the bump peak over the analysis slot time (mean activity of the wedge neuron 16, $\langle r_E^{(16)}(t) \rangle$). In case of no oscillations, this value should be equivalent to the maximum bump peak in panel D. During oscillations, the value closely represents the center of oscillations. Note that between isolines $w_{EE}^{(16,sum)} = 2$ and $w_{EE}^{(16,sum)} = 2(1 + \sqrt{\theta/r_0})$ this value is lower than r_0 . **F** Mean activity over the analysis time slot of ring neurons, $\langle r_I(t) \rangle$. Below the isline $w_{EE}^{(16,sum)} = 2(1 + \sqrt{\theta/r_0})$ the activity of ring neurons increases. Above the isline, the activity of ring neurons first decreases and then rapidly increases. We clipped the values of the mean activity above 100 to facilitate visualization, but the increment of activity in this area reached values over 1000.

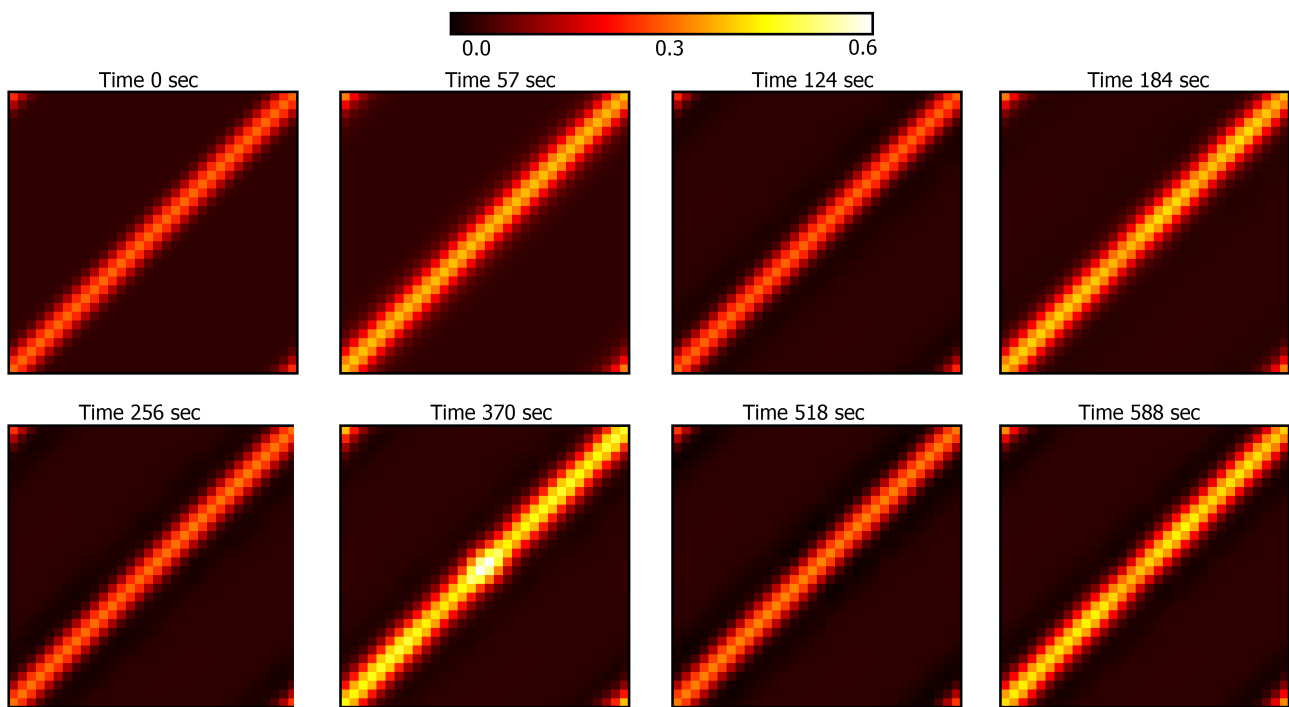


Figure S7. Values of the synaptic weights $w_{EE}^{(ij)}$ in the simulation of Figure 3. From left to right and from top to bottom: each plot shows the values each time there is a switch between wake and sleep phase and *vice versa*. Top, left: initial values of the weights set by the initial values of $w_{EE}^{(max)}$ and σ in Table S2. Top, center left: weights at the end of the first wake phase. Top, center right: after the subsequent sleep phase. Top, right: after the second wake phase. Bottom, left: weights after the second sleep phase. Bottom, center left: after sleep deprivation. Bottom, center right: after sleep rebound. Bottom, right: weights after the third wake phase. Note how the weights after each wake phase are increased (specially after sleep deprivation in the sixth plot) and how the sleep phase resets the weights to close to the initial conditions.

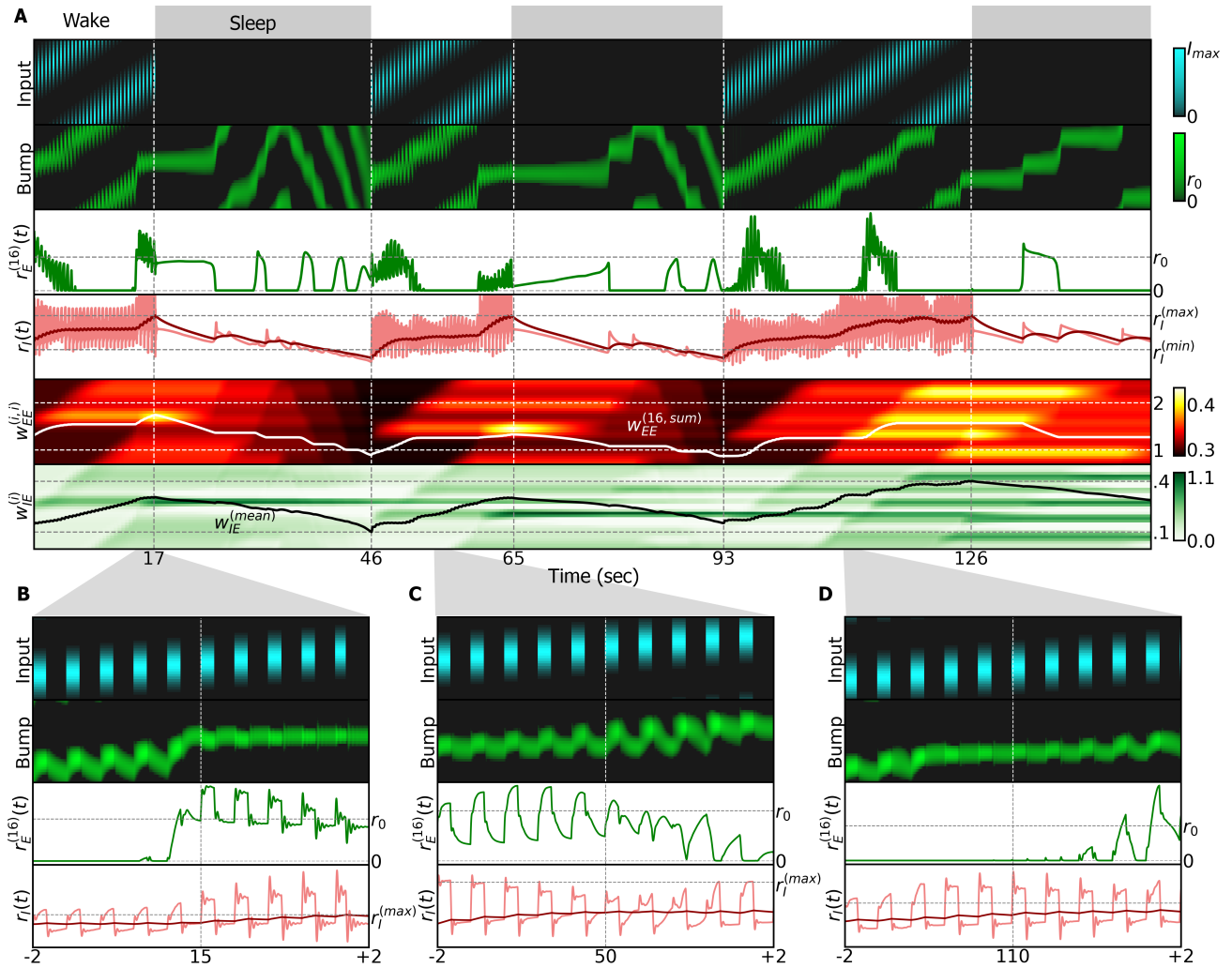


Figure S8. Simulation of the ring attractor network with flashing input during the wake phase (details in Methods(4.9)). **A** Simulation with three wake phases and three sleep phases. A flashing input that turns on and off is provided during the wake phase. During the off period, the ring attractor sustains a bump of activity that drifts due to changes in the synaptic weights $w_{EE}^{(ij)}$. **B** Zoom-in around 15 seconds in the first wake phase of the simulation. **C** Zoom-in around 50 seconds in the second wake phase. **D** Zoom-in around 110 seconds in the third wake phase.

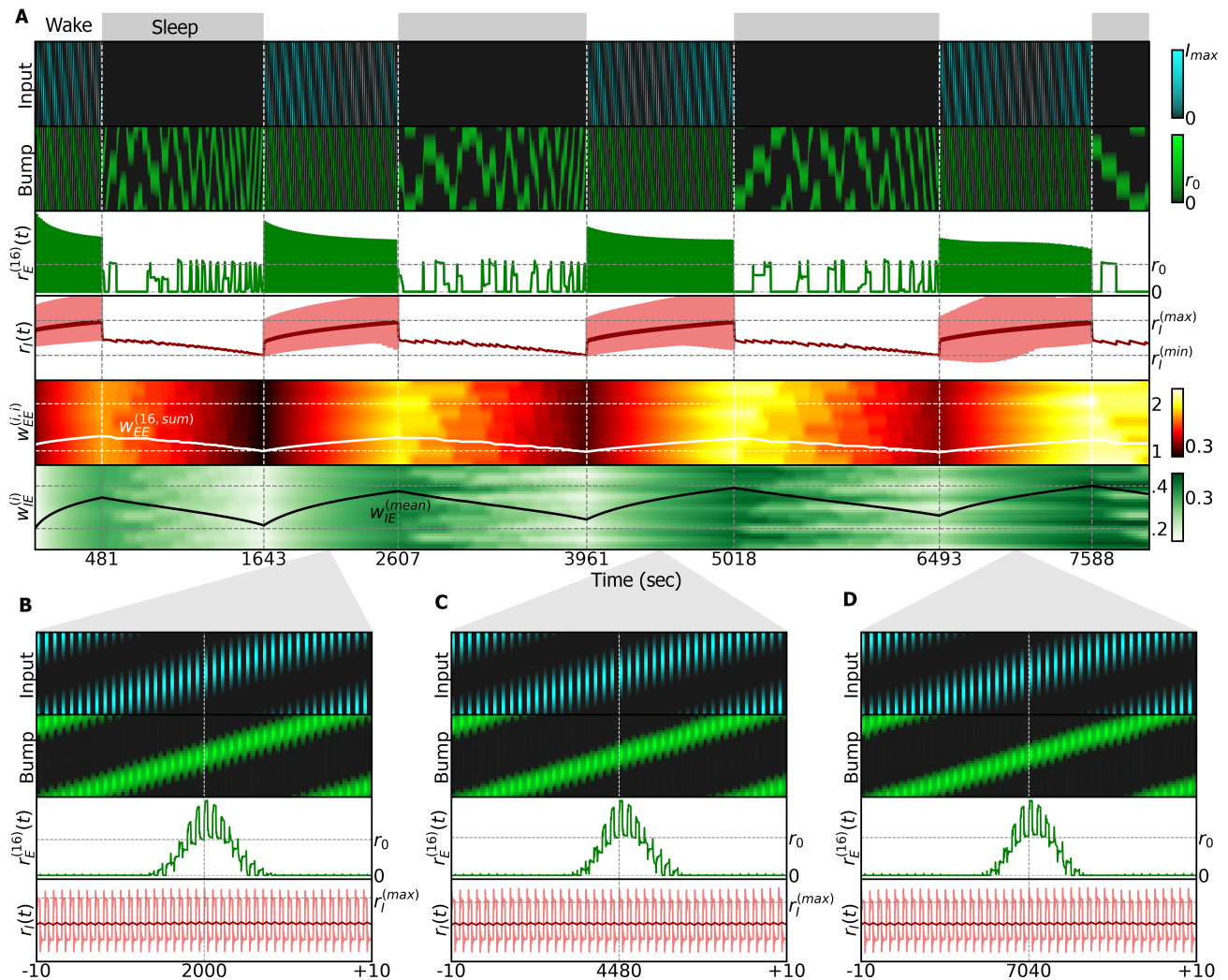


Figure S9. Simulation of the ring attractor network with flashing input during the wake phase with slow plasticity time constants (details in Methods(4.9)). The time constants in this simulation are 100 times larger than in the previous ring attractor simulations. **A** Full simulation with three wake phases and three sleep phases. We used the same input rotation frequency as in Figure S7. As in Figure S7, we provide a flashing input that turns on and off during the wake phase. **B** Zoom-in around 2000 seconds in the first wake phase of the simulation. **C** Zoom-in around 4480 seconds in the second wake phase. **D** Zoom-in around 7040 seconds in the third wake phase. Note how the duration of sleep and wake phases are now in the order of hours due to the increased time constants in the plasticity rules. Note also how the bump of activity is sustained in place without drifting after the input switches off.